Contents lists available at ScienceDirect

Physics of the Earth and Planetary Interiors

Electrical conductivity imaging of the Philippine Sea upper mantle using seafloor magnetotelluric data

Kiyoshi Baba [a,*], Hisashi Utada [a], Tada-nori Goto [b,c], Takafumi Kasaya [c,a], Hisayoshi Shimizu [a], Noriko Tada [c,a]

[a] *Earthquake Research Institute, University of Tokyo, 1-1-1, Yayoi, Bunkyo-ku, Tokyo 113-0032, Japan*
[b] *Graduate School of Engineering, Kyoto University, Kyoto daigaku-Katsura, Nishikyo-ku, Kyoto 615-8540, Japan*
[c] *Institute for Earth Evolution, Japan Agency for Marine-Earth Science and Technology, 2-15, Natsushima, Yokosuka, Kanagawa 237-0061, Japan*

ARTICLE INFO

ABSTRACT

We performed a three-year seafloor electromagnetic survey in the Philippine Sea, including the western edge of the Pacific Ocean, to image electrical features of a deep mantle slab stagnating in the transition zone and the surrounding mantle in three dimensions (3-D). The project iterated one-year deployment of ocean bottom electromagnetometers (OBEMs) using a total of 37 instruments installed at 18 sites. The data obtained have been analyzed in the order of their recovery based on a magnetotelluric (MT) method. In this study, we attempt to obtain a one-dimensional (1-D) electrical conductivity model beneath the Philippine Sea and the Pacific region separately that can be used as a reference model in the first step toward the 3-D analysis. The resultant 1-D models show three main features: (1) The conductivity in the shallower 200 km of the upper mantle depths of the two regions contrasts sharply, which is qualitatively consistent with the large difference in lithospheric age. (2) The conductivity at 200–300 km depth in both regions is more or less the same at approximately $0.3\,\mathrm{S\,m^{-1}}$. (3) The conductivity just below 400 km depth is higher for the Philippine Sea mantle than for the Pacific mantle. The conductivity structure can be interpreted in terms of the thermal structure, mantle hydration, and existence of partial melt using experimental results for the conductivity of mantle minerals. If the conductivity is interpreted simply as the effect of temperature, the mantle beneath the Philippine Sea could be hotter than the dry solidus of mantle peridotite and thus partially molten. However, beneath the Pacific region, the present analysis suggests that the partial melting is not required under the assumed peridotitic composition even if we consider mantle hydration.

© 2010 Elsevier B.V. All rights reserved.

1. Introduction

The Western Pacific area is a field of significant mantle downwelling. The old Pacific plate (125–150 Ma) subducts at the Kurile–Japan, Izu–Bonin, and Mariana trenches. The slabs penetrating into the mantle beneath the back-arc regions were imaged as high-velocity anomalies by seismic tomography (e.g., Fukao et al., 2001; Obayashi et al., 2009). The high-velocity anomalies tend to be distributed horizontally in the mantle transition zone (MTZ). Such anomalies are called stagnant slabs. The stagnation mechanism is not fully understood; thus, it is an interesting topic for mantle dynamics studies. Back-arc basin processes should be related to the

subduction and stagnation of oceanic plates, making them another interesting target to study. As a part of the Stagnant Slab Project (SSP; see the home page, http://ohp-ju.eri.u-tokyo.ac.jp/tokuteiE/), we conducted seafloor electromagnetic (EM) observations in collaboration with seismic observations in the Philippine Sea and on the western edge of the Pacific plate (Shiobara et al., 2009). The EM observations aim to image electrical features of the slab and the surrounding mantle in three dimensions (3-D) with a resolution higher than that available with a semi-global approach (Shimizu et al., 2010b).

The electrical conductivity of the mantle minerals depends strongly on temperature, composition (including the degree of mantle hydration), and the fraction and connectivity of the melt (if the mantle is partially molten). It can change by orders of magnitude with these parameters, and seismic velocities can change by several percent. Because the dependency of the electrical conductivity differs from that of seismic velocities, the electrical conductivity can provide independent information on these parameters. High-velocity anomalies imaged by seismic tomography have

* Corresponding author.
E-mail addresses: kbaba@eri.u-tokyo.ac.jp (K. Baba), utada@eri.u-tokyo.ac.jp (H. Utada), tgoto@tansa.kumst.kyoto-u.ac.jp (T.-n. Goto), tkasa@jamstec.go.jp (T. Kasaya), shimizu@eri.u-tokyo.ac.jp (H. Shimizu), norikot@jamstec.go.jp (N. Tada).
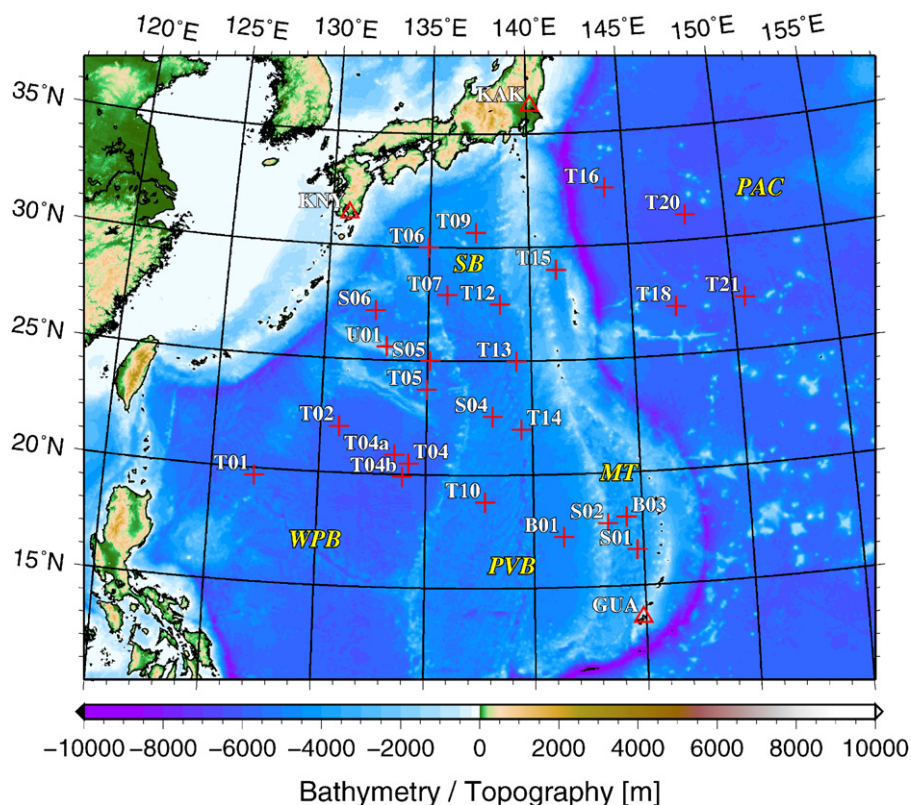
Fig. 1. Location of the seafloor MT sites (red crosses) superimposed on a bathymetric map. The sites whose name starts with T, B, S, and U are those collected through the SSP and from other experiments (Baba et al., 2005; Seama et al., 2007; Utrada et al., 2005), respectively. Red triangles mark the location of geomagnetic observatories from which data were used as remote references for the response estimation. PAC, Pacific Plate; MT, Mariana Trough; SB, Shikoku Basin; PVB, Parece Vela Basin; WPB, West Philippine Basin.

been interpreted as a result of low-temperature perturbations resulting from the presence of cold slab materials. However, it is necessary for further understanding of the mantle status to separate temperature perturbation from other effects. Electrical conductivity can be used for this purpose by joint interpretation using seismic velocities, as reported by Fukao et al. (2004), Ichiki et al. (2006), and Utada et al. (2009).

Studies of mantle conductivity beneath the Philippine Sea have been conducted since the mid-1980s. Pioneering work by Toh (1993) and Utada et al. (1986, 1996) depicted a resistive litho-spheric mantle over a conductive asthenospheric mantle beneath the Shikoku Basin. Utada et al. (1986, 1996) demonstrated that a highly conductive layer appears at a depth of 30 km, whereas it appears as deep as 150 km below the western Pacific basin. Toh (1993) confirmed this feature and proposed a two-dimensional (2-D) conductivity model crossing the Izu–Bonin arc in which the resistive layer of the Pacific is four times as thick as that of the Philippine Sea. Recently, Seama et al. (2007) reported one-dimensional (1-D) conductivity models at five different locations in the Philippine Sea and discussed the relationship between the conductivity model and the tectonic setting and lithospheric age at each site. In the central Mariana area, a linear array study cross-ing the Mariana trench, arc, and back-arc spreading axis (Mariana Trough) was conducted, and the 2-D conductivity structure of the upper mantle was imaged (Baba et al., 2005; Matsuno et al., 2010).

In this study, we introduce seafloor EM observations of the SSP and demonstrate representative 1-D electrical conductivity struc-ture models for the Philippine Sea mantle and the Pacific mantle, which fit all available data observed on either of the oceanic plates. The 1-D analysis is a significant step toward future 3-D inver-sion analysis, because fast and stable conversion of 3-D inversions should be possible using a good representative 1-D model as a start.

We also describe a procedure for correcting data for the effect of land-ocean distribution and bathymetric change, which is critical for obtaining a reliable conductivity model for the mantle.

We describe seafloor EM observations by the SSP and the col-lected data in Section 2. In Section 3, we summarize the method for estimating a 1-D electrical conductivity structure model taking into account the correction for the effect of surface heterogeneity on the observed data. Then, we present the results in Section 4 and dis-cuss the conductivity distribution and its interpretation in Section 5.

2. Observation and data

The present seafloor EM observation iterated one-year deploy-ment of ocean bottom electromagnetometers (OBEMs) using a total of 37 instruments installed at 18 sites on the Philippine Sea plate and the western edge of the Pacific plate (Shiobara et al., 2009). Pre-vious studies cover the area with only a few numbers of seafloor stations (e.g., Baba et al., 2005; Seama et al., 2007) or are based on observations by land geomagnetic stations and submarine cables for basin-scale analysis. These existing data sets do not supply enough information to resolve the geometry of the slab, which shows seismic velocity heterogeneity at a scale on the order of 100 km (e.g., Fukao et al., 2001; Obayashi et al., 2009). Thus, we arranged a 2-D observation array with station intervals of roughly 300 km (Fig. 1). Although it is difficult to establish a sufficient num-ber of nearly permanent observation stations on the seafloor (cf. Toh et al., 2006), iterative maneuver observations using the OBEMs enabled us to acquire the data needed to probe down to the MTZ. The Earthquake Research Institute (ERI), University of Tokyo and Institute for Research on Earth Evolution (IFREE), Japan Agency for Marine-Earth Science and Technology (JAMSTEC) have supplied the

Table 1
Information on the observation sites. E and M in the data status indicate electric field and magnetic field, respectively.

Site	Obs. phase	Latitude	Longitude	Depth (m)	Data status
T01	1	19°41.21′N	127°00.99′E	5284	M only
	2[a]	19°41.52′N	127°01.02′E	5296	E, M
	3	19°41.36′N	127°00.98′E	5283	E, M
T02	1[a]	22°02.65′N	130°52.66′E	5881	E, M
	2	22°02.75′N	130°52.33′E	5841	E[b], M
	3	22°02.58′N	130°52.42′E	5852	E, M
T04a	2	20°51.87′N	133°30.60′E	5909	E[b], M
T04b	2	19°53.65′N	133°53.25′E	5938	E, M
T04	1	20°30.18′N	134°11.82′E	5946	E, M
	2[a]	20°30.29′N	134°11.61′E	5938	E, M
T05	1[a]	23°44.15′N	134°59.62′E	4849	E, M
	2	23°43.93′N	134°59.85′E	4863	E[b], M
	3	23°44.03′N	134°59.54′E	4852	E, M
T06	1[a]	29°59.32′N	134°58.30′E	4629	E, M
	2	29°59.50′N	134°58.63′E	4618	E, M
	3	29°59.56′N	134°58.12′E	4617	E, M
T07	3[a]	27°53.92′N	135°55.37′E	5258	E, M
T09	1[a]	30°39.93′N	137°19.30′E	4270	E, M
	3	30°39.81′N	137°18.82′E	4209	E, M
T10	1[a]	18°47.82′N	137°46.21′E	5354	E, M
	2	18°47.82′N	137°46.05′E	5349	E, M
	3	18°47.81′N	137°46.15′E	5343	E, M
T12	1[a]	27°30.01′N	138°30.83′E	4715	E, M
	2	27°29.83′N	138°30.76′E	4686	E, M
	3	27°29.92′N	138°30.70′E	4697	E, M
T13	1[a]	24°58.70′N	139°17.74′E	4794	E, M
	3	24°58.35′N	139°17.97′E	4785	E, M
T14	1	22°00.00′N	139°29.93′E	4945	E, M
	2[a]	22°00.06′N	139°29.87′E	4941	E, M
	3	21°59.99′N	139°29.95′E	4920	E, M
T15	1[a]	28°59.76′N	141°18.92′E	4026	E, M
T16	3[a]	32°31.19′N	143°57.31′E	5408	E, M
T18	2[a]	27°08.43′N	147°10.29′E	5594	E, M
	3	27°08.58′N	147°10.05′E	5576	E, M
T20	3[a]	31°06.91′N	147°59.87′E	6085	E, M
T21	2	27°18.41′N	150°36.26′E	5911	E, M
	3[a]	27°18.47′N	150°35.85′E	5850	E, M

[a] Data from the observation phases were analyzed in this study.
[b] Data that contain anomalously noisy sections.

project with OBEMs. The OBEMs measure temporal variations in three components of the magnetic field, two horizontal components of the electric field, and two components of the instrumental tilt every minute for a year. Detailed instrumental specifications are described by Kasaya et al. (in preparation).

Iterative observations were conducted through four cruises using a research vessel belonging to JAMSTEC and hiring a working vessel between 2005 and 2008. In the first phase, we deployed 11 OBEMs in October 2005 and recovered them in November 2006. We deployed another 12 OBEMs and started the second phase. The OBEMs were recovered and the third phase was initiated with 14 OBEMs in November 2006. We successfully completed the iterative observations with the recovery of the 14 OBEMs in November 2008. The site and data status for each observation phase are listed in Table 1. The observations were iterated three times for seven sites (T01, T02, T05, T06, T10, T12, and T14) and twice for five sites (T04, T09, T13, T18, and T21), and conducted just once at six sites (T04a, T04b, T07, T15, T16, and T20). At sites where the observations were iterated, the OBEM position was different for each deployment because OBEMs were deployed by free fall from the sea surface. However, the differences are within several hundred meters at most, which can be neglected for mantle structure imaging if the difference in sensitivity between the instruments is negligible. The use of repeated time series as a set of continuous records was tested. The data quality is good for almost all the sites. Anomalously noisy sections are seen in the electric field data of the entire duration at T01 for the first observation phase and for some of the duration at sites T02, T04a, and T05 for the second observation phase.

We processed the raw data in the order of their recovery. In this study, only the data for one observation phase (mainly the first) from 16 sites were used for the following analysis to demonstrate preliminary results. The effect of data accumulation over two or three observation phases is partly demonstrated in Kasaya et al. (in preparation), and more complete analysis will be reported in the future. We used eight additional data sets obtained by past experiments (Baba et al., 2005; Seama et al., 2007; Utrada et al., 2005) to cover the area more densely.

First, the time series of the observed EM field was edited to remove abnormal fluctuations such as spikes and steps. Then, the instrumental clock shift and tilt were corrected. The coordinate system of the data was adjusted to a geographical one in which the x, y, and z directions are northward, eastward, and vertical downward, respectively. The International Geomagnetic Reference Field (IGRF; IAGA, 2005) was used for declination correction. For the electric field data, drift longer than three days was removed by polynomial fitting. Quasi-periodic solar daily variation (Sq), its harmonics, and ocean tides for each time series component were removed by fitting sinusoids for these periods as reported by Lizarralde et al. (1995). The cleaned data were processed into position- ($\mathbf{r}$-) and period-(T-) dependent tensors, $\mathbf{Z}(\mathbf{r}, T)$, relating the horizontal electric and magnetic field spectra, $\mathbf{E}(\mathbf{r}, T)$ in μV m^{-1} and $\mathbf{B}(\mathbf{r}, T)$ in nT, respectively, as shown in (1), using a remote reference and the bounded influence algorithm described by Chave and Thomson (2004).

$$\begin{bmatrix} E_x(\mathbf{r}, T) \\ E_y(\mathbf{r}, T) \end{bmatrix} = \begin{bmatrix} Z_{xx}(\mathbf{r}, T) & Z_{xy}(\mathbf{r}, T) \\ Z_{yx}(\mathbf{r}, T) & Z_{yy}(\mathbf{r}, T) \end{bmatrix} \begin{bmatrix} B_x(\mathbf{r}, T) \\ B_y(\mathbf{r}, T) \end{bmatrix}. \tag{1}$$
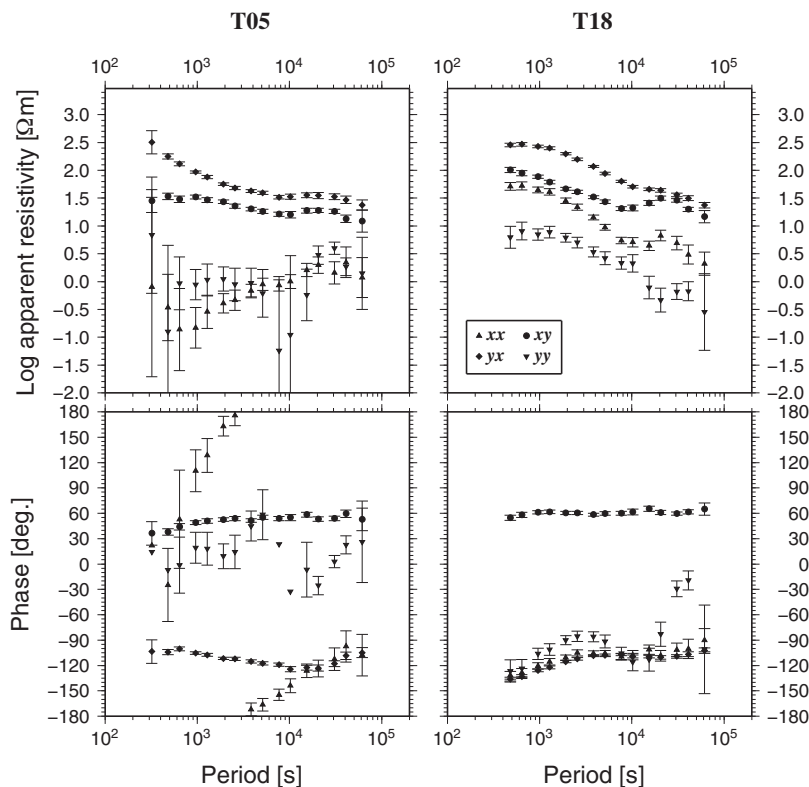
Fig. 2. Examples of the observed MT response at sites T05 and T18. Error bars indicate 95% confidence limits.

Magnetic field data obtained at geomagnetic observatories on land (KAK: Kakioka, KNY: Kanoya, and GUA: Guam) were used as the remote reference. As a result, magnetotelluric (MT) impedance tensors were obtained for periods ranging between 240 and 64,400 s for the 24 sites.

MT responses are illustrated in several ways to demonstrate their features. Each element of the MT impedance tensor for a specified site is frequently plotted to the period, transforming it into the apparent resistivity and impedance phase, defined as

$$\rho_{ij}(\mathbf{r}, T) = \frac{T}{5}|Z_{ij}(\mathbf{r}, T)|^2, \tag{2}$$

$$\phi_{ij}(\mathbf{r}, T) = \tan^{-1}\left\{\frac{\Im Z_{ij}(\mathbf{r}, T)}{\Re Z_{ij}(\mathbf{r}, T)}\right\}, \tag{3}$$

where the subscript i or j corresponds to x or y, respectively. The period dependency of the MT responses are clearly seen in Fig. 2. Here, sites T05 and T18 are selected as the representatives of sites on the Philippine Sea plate and the Pacific plate, respectively. The apparent resistivities have a decreasing trend with increasing period. However, they are higher and their slopes between 1000 and 10,000 s are steeper for T18 than for T05.

The spatial variation of the MT responses can be visualized by polar diagrams of the MT impedance in the dimension of log apparent resistivity and phase tensor ellipses (Caldwell et al., 2004) on the map for a specified period, as shown in Fig. 3. Both the polar diagram and the phase tensor ellipses depict information about the lateral heterogeneity of the electrical conductivity structure, but in different senses. The polar diagram for off-diagonal elements and the phase tensor ellipse become perfect circles and the polar diagram for diagonal elements vanishes if the data are noise-free and the structure is 1-D. The phase tensor ellipse is free from electric field galvanic distortion, in which galvanic charges accumulated in small (compared to inductive scale length) heterogeneous structures near observation sites obscure the data features for regional

structure, because the distorted electric field is approximately in-phase with the regional field (Caldwell et al., 2004). Consequently, the phase tensors may provide more direct information on the regional structure, although magnetic field galvanic distortion also appears to be important for seafloor MT data, which is more significant for periods shorter than several thousand seconds (Chave and Smith, 1994). Swift's impedance skews (Swift, 1967) and phase tensor skew angles, which both indicate the three-dimensionality of the electrical conductivity structure, are also shown by colors in Fig. 3.

We see primary features of the observed MT responses in Figs. 2 and 3. The apparent resistivities show a decreasing trend with an increasing period. However, the tendency is greater for the sites on the Pacific plate than for those on the Philippine Sea plate on average, although the MT responses for sites on the Philippine Sea plate vary more than those on the Pacific plate (Fig. 3). Thus, from these features, the uppermost Pacific mantle is inferred to be more resistive than that beneath the Philippine Sea. Since the Pacific plate is much older than the Philippine Sea plate (Müller et al., 2008), this observation probably indicates that the cool, resistive lithosphere should be thicker for the Pacific mantle than for the Philippine Sea mantle. Meanwhile, for longer periods, the dimensions of the polar diagrams and the phase tensor ellipses are similar among the sites, and the impedance skew values and phase tensor skew angles are smaller, suggesting that the conductivity of the asthenospheric mantle is not greatly laterally heterogeneous.

The eastern sites of the Shikoku–Parece Vela Basin (T09, T12, T13, and T14) have relatively higher Swift skews, while the phase tensor skew is smaller. Similar features but with an opposite sense in the E–W direction are observed for the responses at sites on the Pacific plate (T16, T18, T20, and T21). These observations are probably related to the galvanic effect on the electric field, although the inductive effect of the surface and subsurface conductivity structure cannot be ruled out. The charge accumulations could be caused
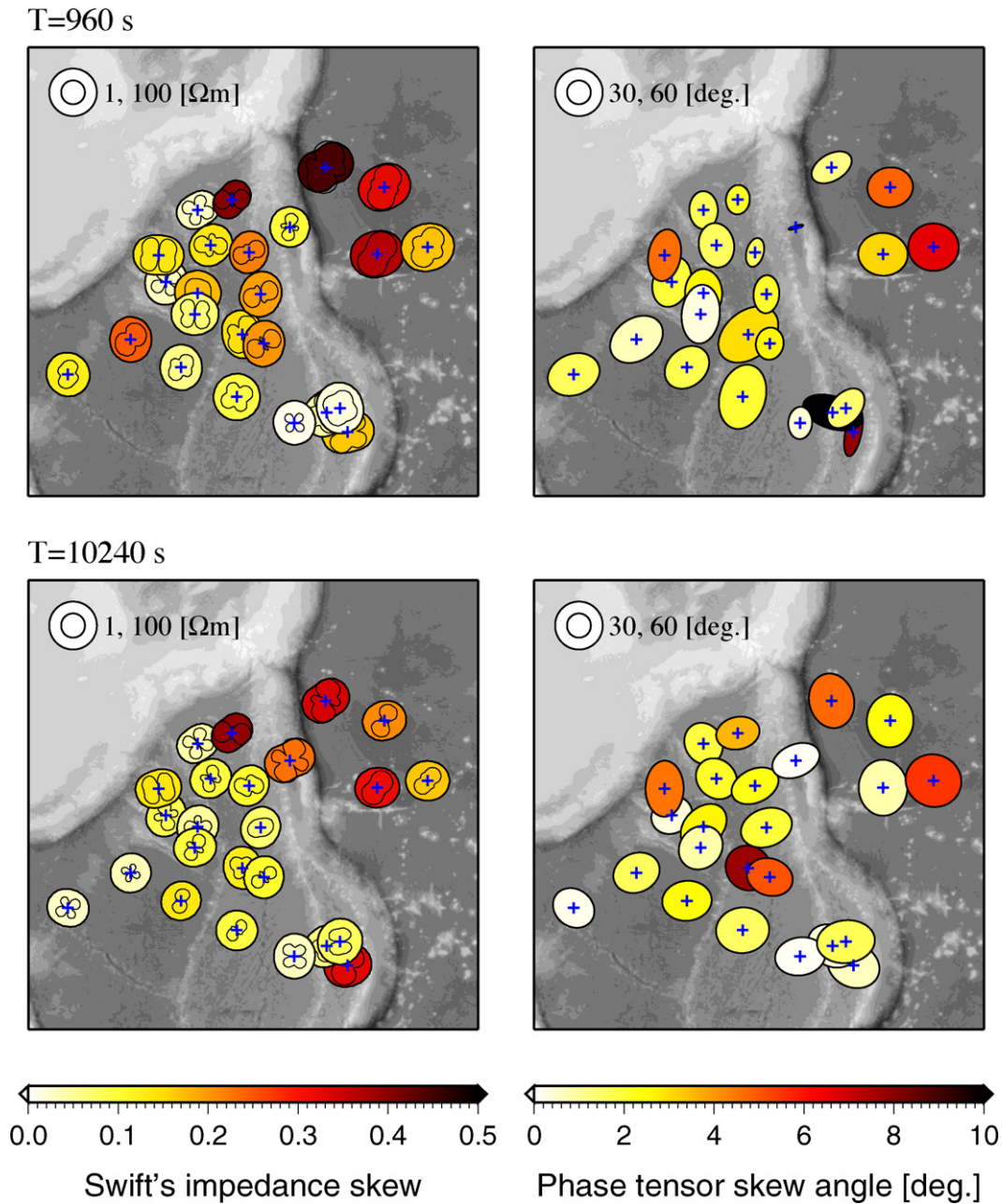
Fig. 3. Polar diagrams of the MT impedances in the dimension of log apparent resistivity, colored by Swift's impedance skew (left), and phase tensor ellipses, colored by the phase tensor skew angle (right) at 960 s (top) and 10,240 s (bottom), superimposed on a topography/bathymetry map (gray shades). For the polar diagrams, thin and thick lines indicate diagonal and off-diagonal elements, respectively. Blue crosses indicate site locations.

by significant bathymetric change, such as that in the Izu–Bonin Trench.

3. Correction for the surface 3-D effect and 1-D inversion

3.1. The correction and inversion iteration procedure

The large contrast in electrical conductivity between seawater and rocks accumulates the boundary electric charges, which can severely distort observed electric and magnetic fields. For marine MT studies, correcting this topographic effect is critical to obtaining accurate conductivity models for the mantle (e.g., Heinson and Lilley, 1993; Nolasco et al., 1998; Baba and Chave, 2005). Baba and Chave (2005) introduced a correction method for seafloor MT data

that combines removal of 3-D topographic effects with inversion of data for 1-D or 2-D structure.

Correction of the surface heterogeneity effect in the present study is essentially based on Baba and Chave (2005) and is summarized briefly below. It is assumed that the effect of surface heterogeneity can be expressed as a complex distortion tensor multiplying the undistorted MT response, so that

$$\mathbf{Z} = \mathbf{Z}_s \mathbf{Z}_m, \tag{4}$$

where $\mathbf{Z}$ is the full (distorted) MT tensor, $\mathbf{Z}_s$ quantifies the distortion due to the surface heterogeneity, and $\mathbf{Z}_m$ is the response caused solely by the underlying regional structure. In a numerical context, $\mathbf{Z}$ and $\mathbf{Z}_m$ can be calculated from an assumed mantle structure, allowing estimation of $\mathbf{Z}_s$. In this study, we want to obtain a 1-D
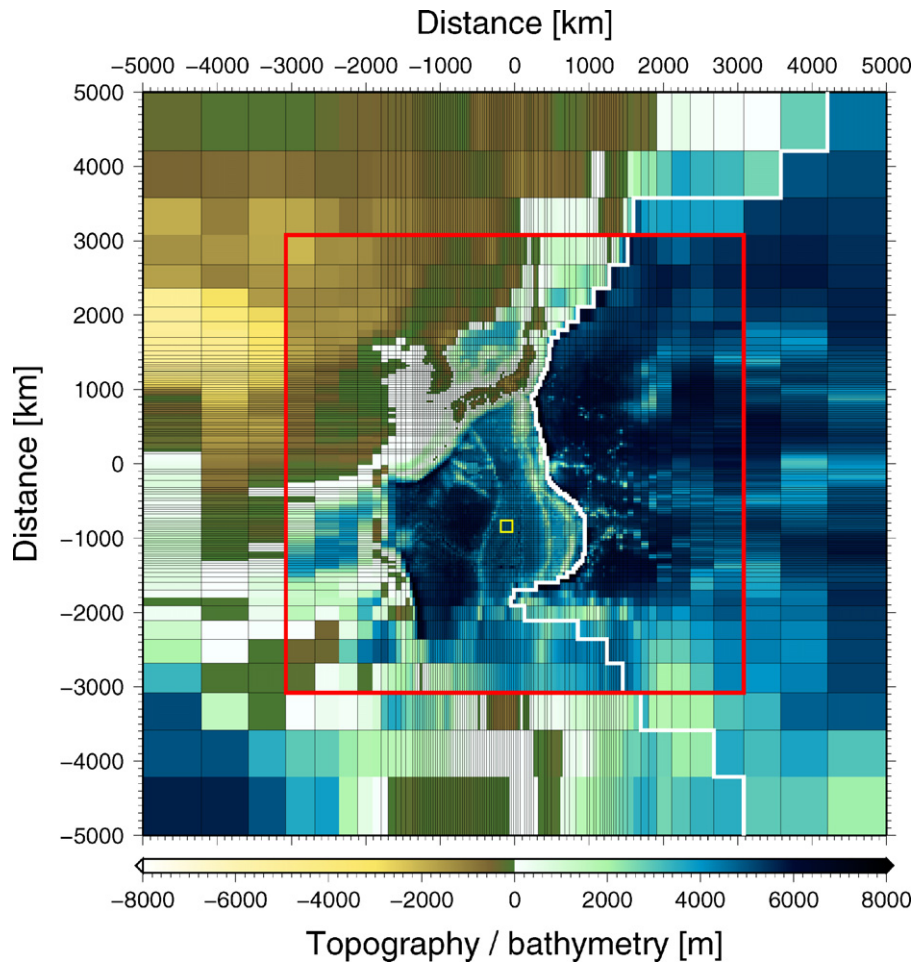
Figure 4. Regional large-scale topography model based on ETOPO2 data. White line indicates the boundary of the Philippine Sea and Pacific 1-D models for forward modeling of the 3-D mantle in Section 5. Yellow box is the area for modeling local-small scale topographic effects for T10, described in Section A.1. Red box shows the area modeled for the test of the horizontal dimension described in Section A.2.

mantle structure; thus, $\mathbf{Z}_m$ is assumed to have the 1-D form,

$$\mathbf{Z}_m = \begin{bmatrix} 0 & Z_{1D} \\ -Z_{1D} & 0 \end{bmatrix}. \tag{5}$$

Defining the observed response $\mathbf{Z}_o$ and the response corrected for the surface heterogeneity effect $\mathbf{Z}_c$ analogously to $\mathbf{Z}$ and $\mathbf{Z}_m$, the observed response may be corrected as follows:

$$\mathbf{Z}_c = \mathbf{Z}_s^{-1}\mathbf{Z}_o = \mathbf{Z}_m\mathbf{Z}^{-1}\mathbf{Z}_o. \tag{6}$$

The numerical modeling method of Baba and Seama (2002), which includes 3-D topography and bathymetry over an arbitrary underlying mantle structure, was used for the forward calculation. This method overcomes the difficulty of directly modeling topography by its transformation into lateral anisotropic conductivity and magnetic permeability changes within the elements in two layers bounding a flattened seafloor. The coupling of deep structure to surface heterogeneity may be checked by iteratively updating the mantle structure using inversion at each step. The convergence of iteration is assessed by the RMS misfit between $\mathbf{Z}_o$ and $\mathbf{Z}$ in the domain of log apparent resistivity and phase,

$$\text{RMS} = \sqrt{\frac{1}{2N_d}\sum_{i=1}^{N_d}\left\{\left[\frac{\log(\rho_{oi}/\rho_i)}{\delta\log\rho_{oi}}\right]^2 + \left[\frac{\phi_{oi}-\phi_i}{\delta\phi_{oi}}\right]^2\right\}}, \tag{7}$$

where $\delta\log\rho_0$ and $\delta\phi_0$ are the estimated standard errors in log apparent resistivity and phase, respectively, and N_d is the total number of data points.

A surface 3-D structure model was created from topography/bathymetry data. We combined two kinds of data sets with different resolutions: 2-min mesh ETOPO2 (NOAA) and a compilation of multi-narrow-beam sounding data (500-m mesh) near the observation sites collected during the SSP cruises and several other JAMSTEC research cruises. A 10,000 km × 10,000 km area centered at 26°20′N, 138°8′E, is discretized into rectangular meshes and incorporated into the 3-D conductivity structure model, assuming mean conductivities for seawater and crustal rock of 3.2 S m^{-1} and 0.01 S m^{-1}, respectively (Fig. 4). In practice, we calculated the EM fields for regional and local models separately and combined them to simulate both effects efficiently. In the appendix, we examine the validity of the combination method for local and regional topographic effects, horizontal dimension of the surface heterogeneity model, and conductivity of the land crust.

We estimate the 1-D conductivity structure by inversion analysis. For 1-D inversion, we need to obtain one scalar MT impedance from the observed MT impedance tensors at all sites. First, we calculate the square root of the determinant of the MT impedance tensor $Z_{det}(\mathbf{r}_i, T)$, defined as

$$Z_{det} = \sqrt{Z_{xx}Z_{yy} - Z_{xy}Z_{yx}}, \tag{8}$$

for each site. Z_{det} is invariant in a horizontal coordinate system and is frequently used to estimate the average 1-D structure (e.g., Seama

et al., 2007). Then, Z_{det} is linearly averaged among the sites,

$$\bar{Z}_{det}(T) = \frac{1}{N_s} \sum_{i=1}^{N_s} Z_{det}(\mathbf{r}_i, T), \qquad (9)$$

where N_s is the total number of sites, and $\mathbf{r}_i$ is the position of the ith site. The standard error of the mean response $\delta\bar{Z}_{det}(T)$ is calculated from the standard errors of the response for each site $\delta Z_{det}(\mathbf{r}_i, T)$, based on the error propagation law:

$$\delta\bar{Z}_{det}(T) = \sqrt{\sum_{i=1}^{N_s} \left| \frac{\partial\bar{Z}_{det}(T)}{\partial Z_{det}(\mathbf{r}_i, T)} \right|^2 \delta Z_{det}^2(\mathbf{r}_i, T)}$$

$$= \frac{1}{N_s} \sqrt{\sum_{i=1}^{N_s} \delta Z_{det}^2(\mathbf{r}_i, T)}. \qquad (10)$$

Note that $\delta\bar{Z}_{det}(T)$ does not indicate the variance of the sampled $Z_{det}(\mathbf{r}_i, T)$ but indicates the variance of the estimated $\bar{Z}_{det}(T)$. We invert the apparent resistivity and phase for $\bar{Z}_{det}$ using an Occam algorithm with a smoothness constraint in terms of the second derivative of the conductivity with depth (Constable et al., 1987).

The iteration procedure starts with the 1-D inversion of $\bar{Z}_{det}$ calculated from the observed (non-corrected) MT responses $\mathbf{Z}_o$, $\bar{Z}_{det}^{0th}$, based on (8) and (9). Hereafter, we use a superscript for $\bar{Z}_{det}$ and $\mathbf{Z}_c$ to specify the iteration number as needed. A 3-D forward modeling consisting of the surface heterogeneity over the 1-D model obtained from $\bar{Z}_{det}^{0th}$ is conducted, and the RMS misfit in (7) is calculated (zeroth iteration). Then, in the first iteration, the effect of the 3-D surface heterogeneity is corrected and $\mathbf{Z}_c^{1st}$ is obtained. The 1-D model is updated by inverting the $\bar{Z}_{det}^{1st}$ calculated from $\mathbf{Z}_c^{1st}$, and 3-D forward modeling with calculation of the RMS misfit is repeated until the process converges.

3.2. Constraints on the resistive lithospheric mantle

Before iterating the correction and inversion, we examine the sensitivity to the conductivity of the resistive part of the uppermost mantle. We can anticipate that the uppermost mantle is relatively resistive because the conductivity of rock decreases under the low-temperature conditions of oceanic lithosphere. For example, Cox et al. (1986) reported resistive lithospheric mantle ($<2 \times 10^{-5}$ S m^{-1} below 5 km depth) beneath the northeastern Pacific on the basis of controlled-source EM sounding. In general, Z_{det} is less sensitive to the presence of a resistive layer than to the presence of a conductive layer, and 1-D inversion with a smoothness constraint cannot correctly reconstruct such a layer. On the other hand, full MT impedance tensors treated in three dimensions are more sensitive to the resistive part, as shown below.

We conducted 3-D forward modeling of the full MT impedance tensors for 20 sites on the Philippine Sea plate and used the result to constrain the conductivity of the lithospheric mantle. Four 3-D models, L1–L4, were prepared, each consisting of a common surface 3-D heterogeneity over a different 1-D mantle structure. The 1-D structure models are obtained by Occam inversion of $\bar{Z}_{det}^{0th}$ with an additional constraint for different conductivities at 20 km depth, imitating the model of Cox et al. (1986) (Table 2 and Fig. 5). For model L1, no constraint was applied at 20 km depth. The inversion produced the smoothest model with a conductivity of approximately 1.3×10^{-2} S m^{-1} at 20 km depth. For models L2, L3, and L4, the conductivity at 20 km depth is constrained to take values of 3.2×10^{-3}, 3.2×10^{-4}, and 3.2×10^{-5} S m^{-1}, respectively.

The uppermost layer is expected to be more conductive than the underlying layer, as suggested by the decreasing trend of the apparent resistivity in the shortest period (Fig. 6). However,

Table 2
RMS misfit between $\mathbf{Z}_o$ and $\mathbf{Z}$ for different 1-D models assumed beneath surface heterogeneity.

Model	Conductivity at 20 km depth (S m^{-1})	RMS misfit				
		xx	xy	yx	yy	Total
L1	1.3×10^{-2}	33.2	12.5	17.4	26.6	23.8
L2	3.2×10^{-3}	31.7	12.2	17.1	24.2	22.6
L3	3.2×10^{-4}	12.7	10.6	16.3	17.1	14.4
L4	3.2×10^{-5}	19.4	21.3	24.7	8.5	19.5

the sensitivity of the MT response to the uppermost layer seems marginal because the conductivity of the uppermost layer changes greatly with the constraints on conductivity at 20 km depth. The conductivity of the uppermost layer is critical for estimating and correcting the local topography effect because the conductivity contrast between seawater and seafloor strongly controls the effect. Thus, it should be constrained *a priori*. The conductivity of the top layer is also constrained to 0.1 S m^{-1} for all the models. This value seems a good approximation of the conductivity of the oceanic crust for the Philippine Sea plate as reported by the MT studies in the Nankai Trough (Goto et al., 2003; Kasaya et al., 2005). A controlled-source EM study on 40 Ma crust in the northeastern Pacific also shows the conductivity varing from 1 S m^{-1} to 0.01 S m^{-1} in 1 km depth below the seafloor (Constable and Cox, 1996). The resultant 1-D models are shown in Fig. 5. All four models fit $\bar{Z}_{det}^{0th}$ with an RMS misfit of unity.

From the result of 3-D forward modeling of surface 3-D heterogeneity effects, we can also calculate the RMS misfit in (7). The resulting misfit is best for the case in which model L3 was incorporated (Table 2). For models L1, L2, and L3, with decreasing conductivity, the misfit improved for all four tensor elements. The improvement for the diagonal elements was especially significant.
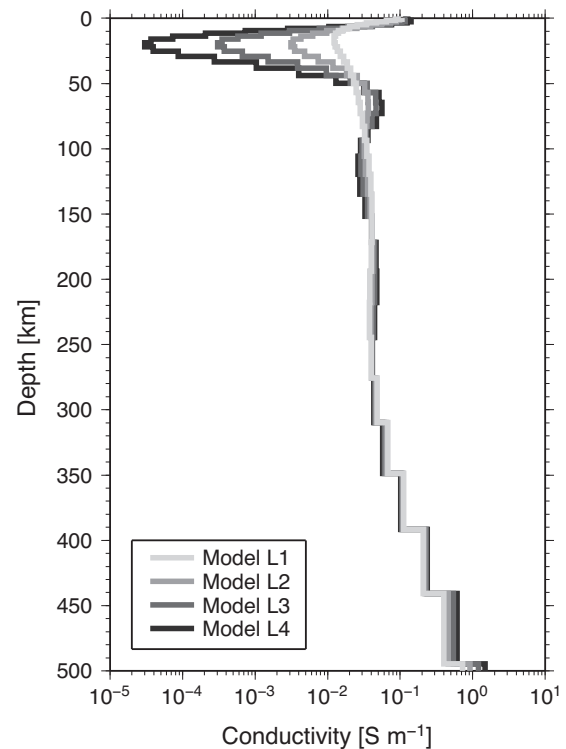

Fig. 5. 1-D mantle conductivity models obtained by inversion with different constraints on the conductivity at 20 km depth. Each model was combined with the 3-D surface heterogeneous model shown in Fig. 4, and 3-D forward modeling was conducted.
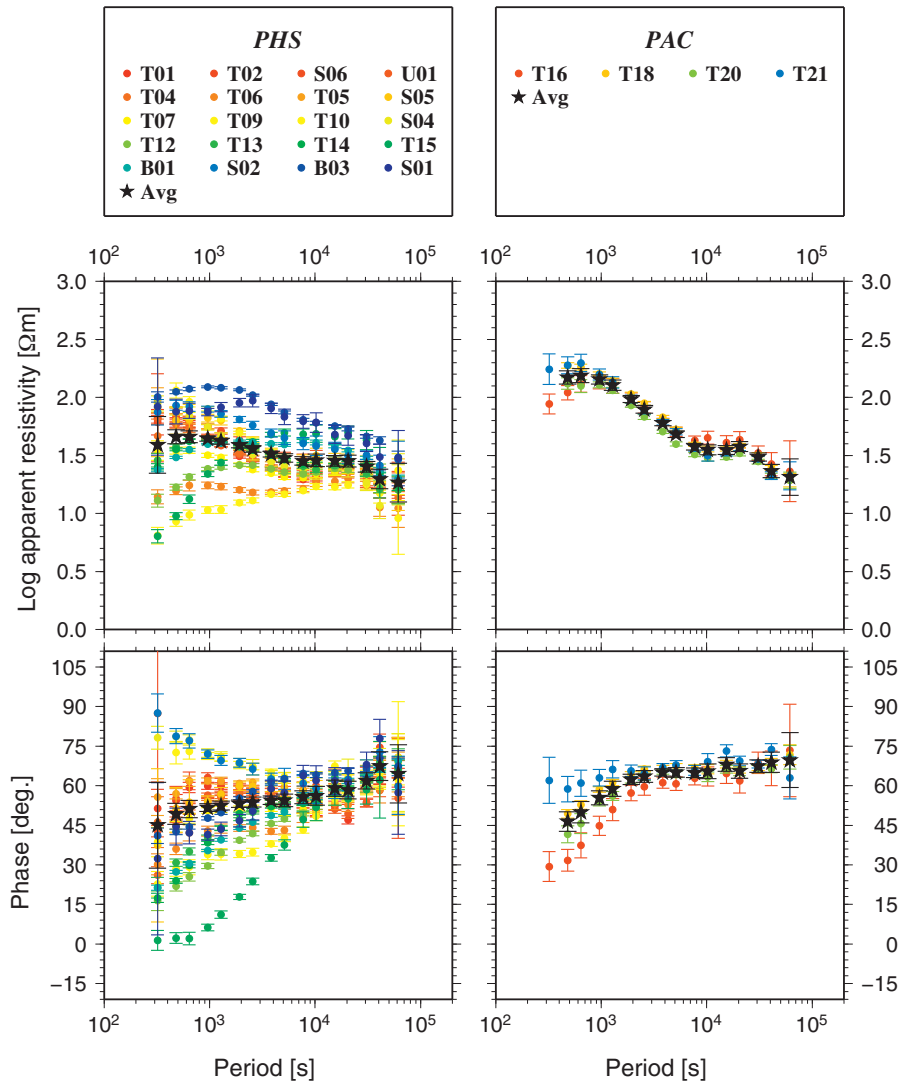
Fig. 6. Apparent resistivity and phase for Z_{det}^{0th} (colored circles) for each site and $\bar{Z}_{det}^{0th}$ (black stars): sites on the Philippine Sea plate (left) and sites on the Pacific plate (right). Error bars indicate 95% confidence limits.

However, for model L4, the misfit for off-diagonal and *xx* elements worsened, although that for the *yy* element was the best. The 3-D features of the MT responses for these models are produced by surface heterogeneity because the subsurface structure is 1-D. The forward modeling results indicate that the three-dimensionality of the MT impedances is more enhanced with decreasing lithospheric mantle conductivity (not shown), and the best fit to the observations is obtained when the conductivity is approximately $3.2 \times 10^{-4}\,\mathrm{S\,m^{-1}}$.

On the basis of the above result, we add the constraints of $3.2 \times 10^{-4}\,\mathrm{S\,m^{-1}}$ at 20 km depth and $0.1\,\mathrm{S\,m^{-1}}$ at the top layer in the 1-D inversion during topographic effect correction and inversion iterations. The topographic effect is calculated on the 3-D structure consisting of the surface heterogeneity over the 1-D model obtained by inversion with the two constrains. The observed MT responses are then corrected for the effect through the procedure described in Section 3.1.

4. Results

We applied the iteration procedure to the data for the Philippine Sea plate and Pacific plate separately because the mantle struc-

ture is expected to differ significantly between the two regions. Fig. 6 shows the apparent resistivity and phase for Z_{det}^{0th} at each site. The features of these responses in the two regions differ, confirming that averaging the responses separately is appropriate. Consequently, the MT responses for 20 and 4 sites are averaged for the Philippine Sea mantle and Pacific mantle, respectively. Clearly, the Z_{det} responses for the Philippine Sea plate vary more, and the apparent resistivities are higher for the Pacific plate than for the Philippine Sea plate, as mentioned for the raw responses in Section 2. Also, unusual features appear in some of the MT responses, especially for the Pacific sites, for which the responses increase very abruptly and cannot be fitted by a 1-D model over periods ranging between several hours and one day. This is probably due to the imperfect removal of Sq and its higher harmonics (Utada et al., 2008). These signals have a scale length comparable with the scale of the conductivity structure of interest, so the plane wave source assumption for MT will be violated. Thus, we cleaned four data points (apparent resistivity at 30,720, 20,480, and 15,360 s and phase at 15,360 s) of $\bar{Z}_{det}$ for the Pacific by replacing them with the model responses of ρ^+ inversion (Parker and Booker, 1996), which places lower and upper bounds on the apparent resistivity and phase consistent with the governing physical dispersion relation.
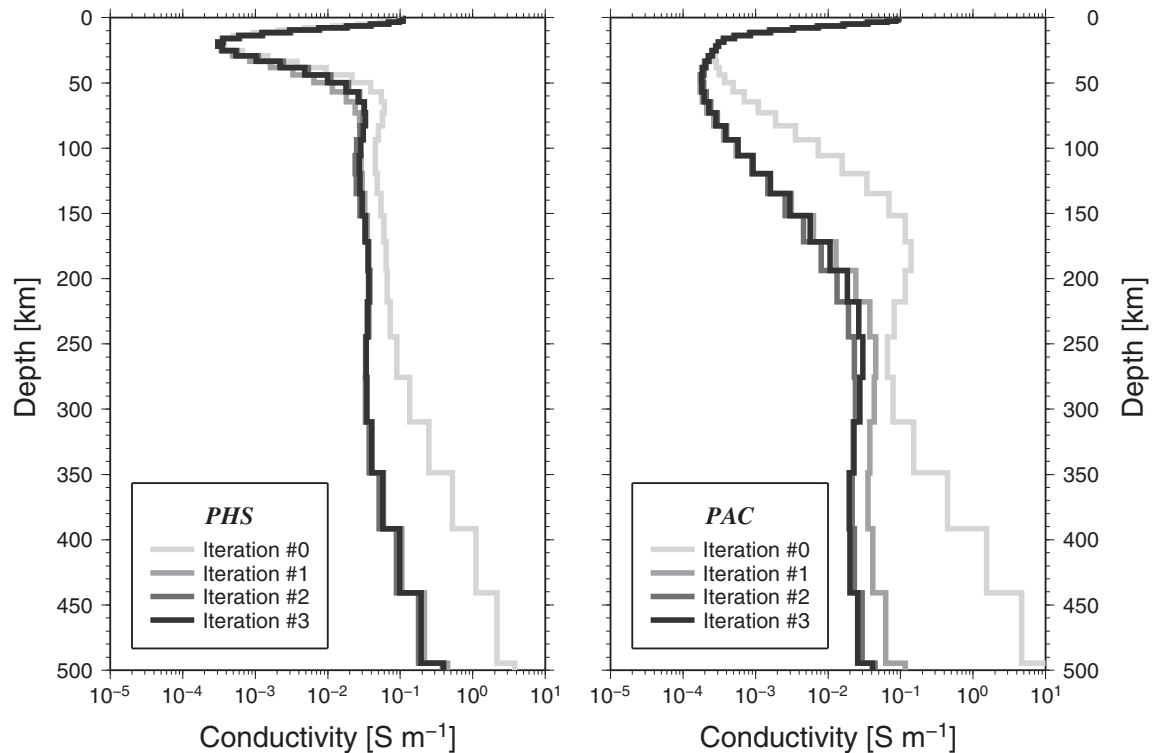
Fig. 7. 1-D mantle models obtained at each iteration stage: Philippine Sea mantle (left) and Pacific mantle (right).

The correction and inversion processes were iterated three times. Both the 1-D model and the RMS misfit changed considerably in the first iteration and lesser in further iterations (Fig. 7). This observation indicates that mutual coupling between the surface heterogeneity effect and the deep mantle structure is not dominant. The 1-D models obtained from the corrected responses are significantly more resistive than those obtained from the non-corrected responses for both the Philippine Sea and Pacific plates. This result can be explained mainly by the effect of ocean/land contrast. We selected the models at the third iteration because the solution is well converged.

The residuals between the observed and modeled responses are plotted in Figs. 8 and 9. For the Philippine Sea mantle, the residuals tend to be distributed around zero, indicating that surface heterogeneity over the 1-D mantle explains all data equally. The variances are greater for shorter periods, suggesting more lateral heterogeneity in the shallower mantle. For the Pacific mantle, the residuals for the xy and yx apparent resistivity are biased in opposite senses. Thus, the split of the xy and yx apparent resistivities cannot be explained only by surface heterogeneity. Lateral heterogeneity in the mantle is strongly expected to be the cause. We discuss this in detail later. Note that the preferred models explain the main features of all four elements relatively well, as also seen in the RMS misfit for model L3 in Table 2.

5. Discussion

5.1. Uncertainty of the conductivity

We estimate the uncertainty of the conductivity for each layer of the preferred 1-D models by the following process: (1) 1-D inversion was conducted 13 times, applying different *a priori* constraints for the conductivity of a specified layer. The constrained value was changed for each run from 10^{-5} to 10^1 S m^{-1} at every 0.5-order step. (2) The first step was iterated for all (44) layers; thus, 572 inversions were performed. (3) The conductivity distribution was

determined by gathering the models that converged with an RMS misfit of unity. Then, two pairs of quantiles (for 15.0% and 85.0% and for 2.5% and 97.5%) were calculated to display the distribution by the 70% and 95% limits. The obtained uncertainty is shown together with the preferred model in Fig. 10a.

The results show that the conductivities in the depth ranges between approximately 150 and 250 km for the Philippine Sea and between approximately 200 and 300 km for the Pacific are distributed in a relatively narrow band, suggesting that the conductivities at these depths are well constrained by $\bar{Z}_{det}$. However, the uncertainty for the upper resistive part is larger and thus not well constrained by $\bar{Z}_{det}$. The distribution is inhomogeneous and asymmetric about its mode value but tends to be broad toward the resistive side. These observations also indicate the potential sensitivity of the scalar MT response mentioned in Section 3. The uncertainty increases approximately below 550 km depth for the Philippine Sea mantle. For the Pacific mantle, it is low up to approximately 700 km depth because of the larger skin depth due to the thick resistive layer in the upper mantle.

5.2. Conductivity for the lithospheric and asthenospheric mantle

The preferred 1-D models (Fig. 10a; hereafter, we call these models D0$_{PHS}$ and D0$_{PAC}$) show that the resistive layer is much thinner for the Philippine Sea mantle than for the Pacific mantle, as expected. The conductivity peaks at depths of approximately 80 km and 250 km, respectively, for each mantle. The large difference in the thickness of the resistive layer is consistent with past studies (Utada et al., 1986, 1996; Toh, 1993) and can be attributed to lithospheric cooling with age. The conductivity for the Pacific mantle is more resistive, and the peak in the conductivity is deeper compared with the northeastern Pacific (Lizarralde et al., 1995) (Fig. 10a). This difference can also be ascribed to lithospheric age. Lizarralde et al. (1995) analyzed electric field data measured by a submarine cable between Hawaii and California corresponding to a seafloor age between 5 and 90 Ma; thus, their model repre-
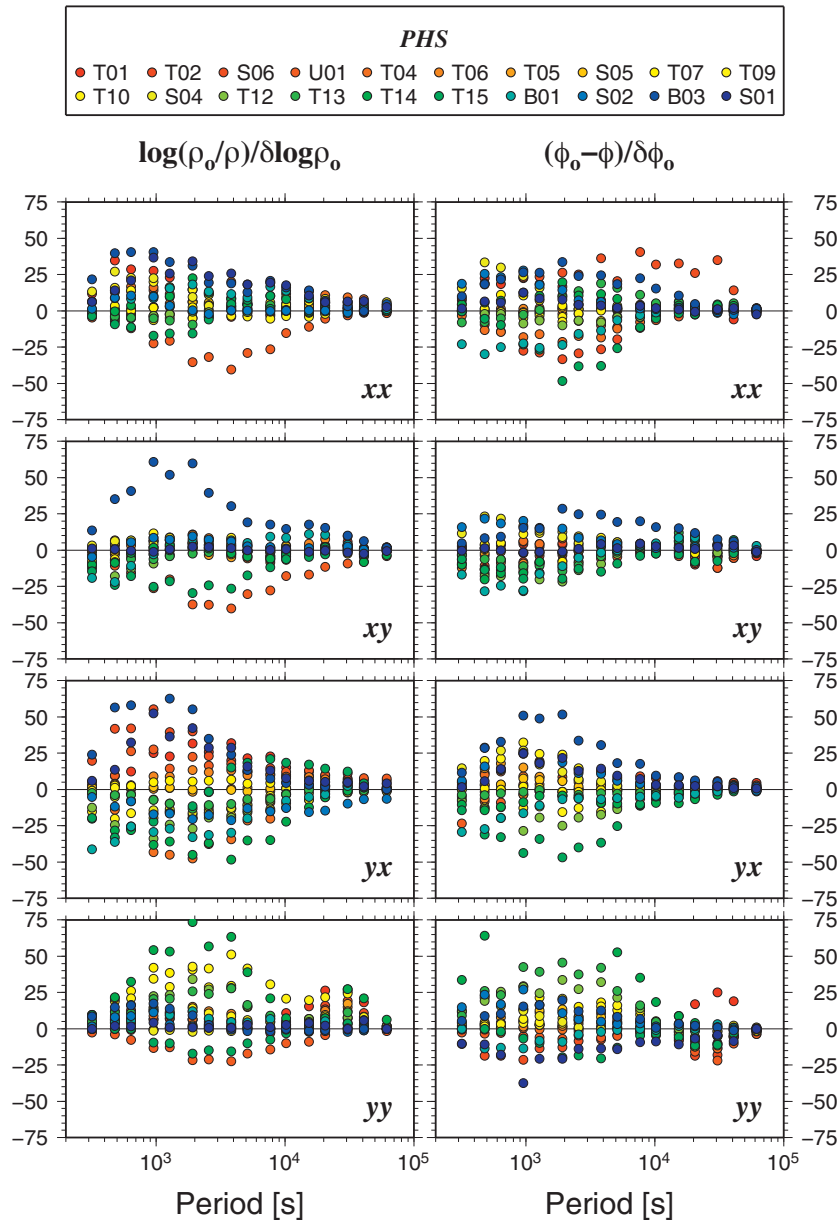
Fig. 8. Residuals between four components of the MT impedance tensors observed and modeled for 20 sites on the Philippine Sea plate. Values are normalized by the estimated standard errors, which are the same as those in (7). Model responses are calculated by 3-D forward modeling of a model consisting of the 3-D surface heterogeneity (Fig. 4) over the 1-D structure obtained by inversion (Fig. 7).

sents a mantle younger than the western Pacific mantle that we studied.

The large difference between the Philippine Sea mantle and the Pacific mantle in the conductivity of the upper 200 km is the first-order lateral heterogeneity. The data observed on the Pacific plate are more sensitive than those observed on the Philippine Sea plate to the 3-D structure caused by lateral variation in the conductivity: a young conductive Philippine Sea mantle appears beyond the plate boundary to the west, partly because the MT data are sensitive to the high-conductivity zone. This speculation is examined by forward modeling. We combined the surface heterogeneous structure and the two preferred 1-D models into a model with a 3-D surface over a 3-D mantle. The two mantle models are bounded at the Kurile–Japan–Izu–Bonin–Mariana trenches (Fig. 4). In other words, models $D0_{PHS}$ (Fig. 10a, red line) and $D0_{PAC}$ (Fig. 10a, blue line) are embedded below the seafloor west and east, respectively, of the white line in Fig. 4. The responses calculated for the 3-D/1-D

and 3-D/3-D models were compared, as shown in Fig. 11, together with the observed responses. For the 3-D/1-D model, the apparent resistivity is larger for the *xy* element than for the *yx* element, which is opposite to the features of the observed response. The diagonal apparent resistivities are almost of the same magnitude as the *yx* apparent resistivity. On the other hand, the response in the 3-D/3-D model recovers the features of the observed response more accurately, although it is not perfect. The relative magnitude of the *xy* and *yx* apparent resistivities is in the same sense as the observations, and the separation of the *xx* and *yy* apparent resistivities increases and becomes closer to the observations. Changes in the responses between the two models are seen in the responses in the Philippine Sea, but these are not as significant as those for the Pacific sites.

The conductivity within the Philippine Sea mantle should vary laterally because the Philippine Sea plate consists of three different tectonic basins formed successively since 60 Ma: the West Philip-
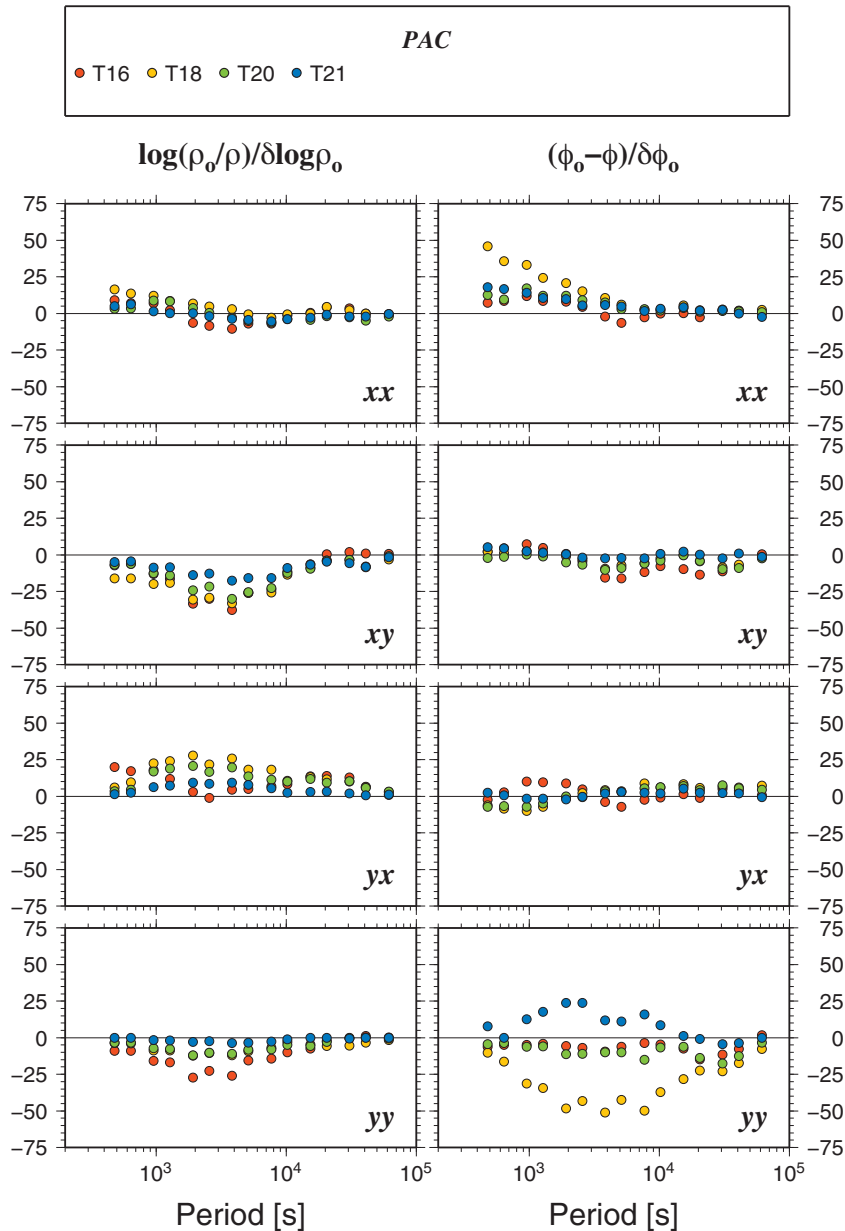
Fig. 9. Normalized residuals between four components of the MT impedance tensors observed and modeled for four sites on the Pacific plate.

pine Basin, the Shikoku–Parece Vela Basin, and the Mariana Trough. Seama et al. (2007) determined the conductivity variation associated with lithospheric age through 1-D inversions of single-site MT data from different basins. The lateral heterogeneity within the plate, which may or may not be related to the lithospheric age, could be beyond the scope of this paper, which aims to produce a reference 1-D model for future 3-D analysis. However, we mention the possible difference between the mantle beneath the Shikoku–Parece Vela Basin and that beneath the West Philippine Basin. The Z_{det} responses after topographic effect correction are averaged for seven sites on the West Philippine Basin and for nine sites on the Shikoku–Parece Vela basin. The averaged responses are separately inverted and compared (Fig. 12). The apparent resistivity at shorter periods is higher for the West Philippine Basin than for the Shikoku–Parece Vela Basin and, correspondingly, the obtained 1-D models show that the resistive layer is thicker for the West Philippine Basin than for the Shikoku–Parece Vela Basin. This trend is consistent with expectation and the report of Seama et al. (2007),

although the difference is not very significant, as the 70% limits of the two models overlap.

In contrast to the uppermost mantle mentioned above, the conductivity below the resistive layer is more similar at approximately $0.3 \, \mathrm{S\,m^{-1}}$ in both these regions and in the northeastern Pacific (Fig. 10a). The conductivities at 80–200 km depths for the Philippine Sea mantle and at 200–250 km depths for the Pacific mantle are relatively robust even if we constrain the conductivity of the layer just above the 400 km discontinuity, as seen in the following section. The robustness is also supported by the narrow uncertainty. Similar conductivity values have been obtained in the Tasman Sea (Heinson and Lilley, 1993) and French Polynesia (Nolasco et al., 1998). Baba et al. (2005) reported that the mantle below the resistive layer beneath the Mariana Trough is three times more conductive than the Pacific mantle, the conductivity of which is almost the same as that obtained in this study ($0.3 \, \mathrm{S\,m^{-1}}$). The apparent inconsistency between the two studies may be the result of local anomalous structure beneath the Mariana Trough, where
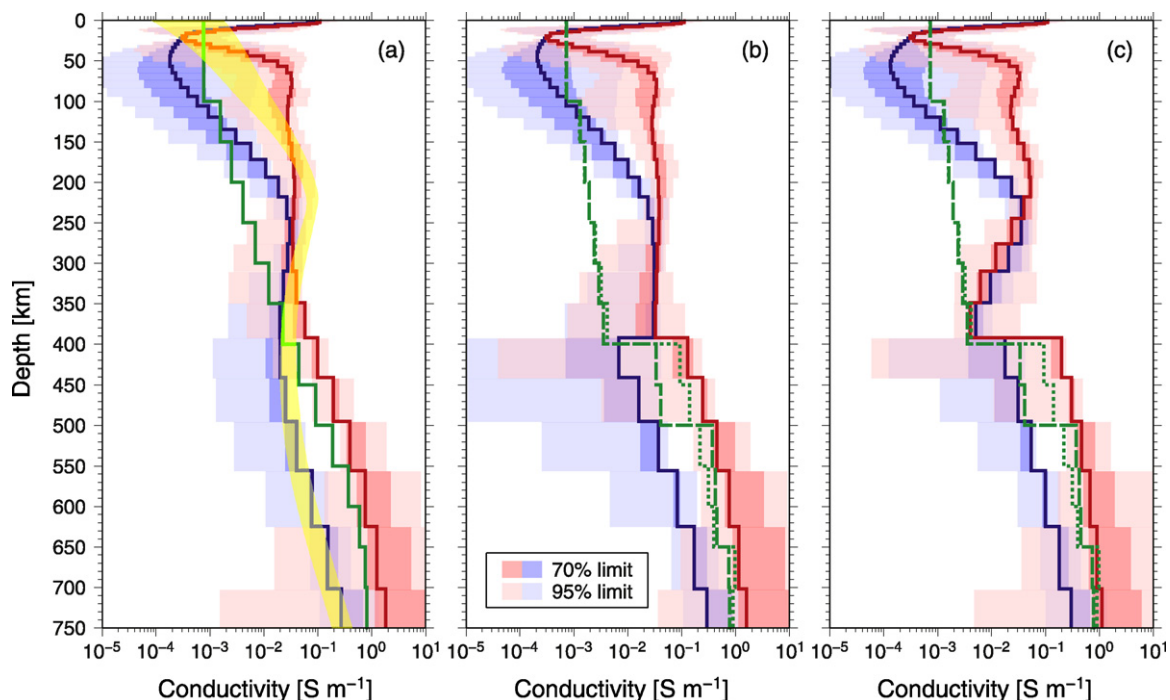
Fig. 10. 1-D conductivity models obtained by inversion with different conditions. Red and blue lines are the models for the Philippine Sea mantle and Pacific mantle, respectively. Shading indicates the uncertainty of the conductivity for each layer. Inset show the distribution limits. Reference 1-D models for the north Pacific obtained by Shimizu et al. (2010a) are also plotted by green solid (smooth model), dotted (two-jump model), and dashed (three-jump model) lines. (a) Preferred models that are the same as that shown in Fig. 7 (models D0$_{PHS}$ and D0$_{PAC}$). Yellow line shows the 1-D model for the northeastern Pacific mantle obtained by Lizarralde et al. (1995). (b) Models obtained by inversions permitting a jump at approximately 400 km depth (models D1$_{PHS}$ and D1$_{PAC}$). (c) Models obtained by inversions permitting the jump and constraining the conductivity just above the jump to 3.2×10^{-3} S m^{-1} (models D2$_{PHS}$ and D2$_{PAC}$).

seafloor is currently spreading (e.g., Yamazaki et al., 2003). The similarity in the conductivity below the resistive layers may suggest that no significant difference exists in the physical and chemical conditions of the asthenospheric mantle between the normal ocean and back-arc basin.

5.3. Conductivity around 400 km depth

The conductivity structure of the MTZ was recently investigated by Shimizu et al. (2010a). They analyzed MT and geomagnetic depth sounding (GDS) responses over periods longer than several days obtained from data collected by trans-Pacific submarine cables and geomagnetic observatories in and around the Pacific Ocean and demonstrated 1-D reference conductivity models for the north Pacific area. The smooth version of their models is shown together with our preferred models D0$_{PHS}$ and D0$_{PAC}$ in Fig. 10a. The conductivity beneath the Philippine Sea at depths of 400–550 km increases gradually with depth from ~0.1 to ~0.4 S m^{-1}, which is higher than the north Pacific reference model. The conductivity beneath the Pacific region in the same depth range is about one order lower than that beneath the Philippine Sea and is also lower than the north Pacific reference. However, it agrees very well with the conductivity beneath the northeastern Pacific obtained by Lizarralde et al. (1995). The difference between models D0$_{PHS}$ and D0$_{PAC}$ is significant even if we consider the models' uncertainties (Fig. 10a).

We next examine the possibility of a conductivity structure discontinuity at approximately 400 km depth. As the seismic velocity changes discontinuously at 410 and 660 km depths due to the phase transition of mantle minerals in the MTZ, the electrical conductivity may also change abruptly at these depths. Experimental studies support a discontinuous enhancement in conductivity due to the phase transition (e.g., Xu et al., 2000). We consider only the upper half of the MTZ, because the MT responses in this study can constrain the mantle structure above 550 km in depth more accurately,

as demonstrated above. The inversion of MT data in the current manner cannot detect such discontinuities because the conductivity structure is constrained to change smoothly with depth. Therefore, we run the inversions with additional sets of *a priori* information.

We invert $\bar{Z}_{det}^{3rd}$ releasing the smoothness constraint (permitting a jump in conductivity) at approximately 400 km depth. The model uncertainties are also calculated as for models D0$_{PHS}$ and D0$_{PAC}$. This analysis is done for both the Philippine Sea data and the Pacific data. The obtained models (D1$_{PHS}$ and D1$_{PAC}$) are shown in Fig. 10b. The calculated responses to these models fit the data as well as the responses to the preferred models D0$_{PHS}$ and D0$_{PAC}$ with the RMS misfits of unity. The conductivities of models D1$_{PHS}$ and D1$_{PAC}$ are very similar at approximately 0.3 S m^{-1} at 300–400 km depth, which is slightly lower (higher) than the conductivity of model D0$_{PHS}$ (D0$_{PAC}$). The conductivity of model D1$_{PHS}$ (D1$_{PAC}$) just below the discontinuity becomes slightly higher (smaller) than that of model D0$_{PHS}$ (D0$_{PAC}$), so the conductivity difference between the two regions is emphasized. Two discontinuous versions of the Pacific reference by Shimizu et al. (2010a) (model with two jumps at 400 and 650 km depth and model with three jumps at 400, 500, and 650 km) both fall between models D1$_{PHS}$ and D1$_{PAC}$. Although the uncertainties, particularly for the 95% limit, are large at 400–550 km depth for both D1$_{PHS}$ and D1$_{PAC}$, the conductivity distributions are not homogeneous, and the 70% limits for the two models do not overlap. Therefore, we can distinguish the two models with high probability. However, the negative jump in conductivity at 400 km depth for model D1$_{PAC}$ is difficult to interpret in terms of the phase change. Above the discontinuity, both D1$_{PHS}$ and D1$_{PAC}$ are higher than the north Pacific references. These inconsistencies are examined by further inversions.

We attempt inversions permitting a jump at approximately 400 km and further constraining the conductivity just above the discontinuity to 3.2×10^{-3} S m^{-1}, which is close to the values of the
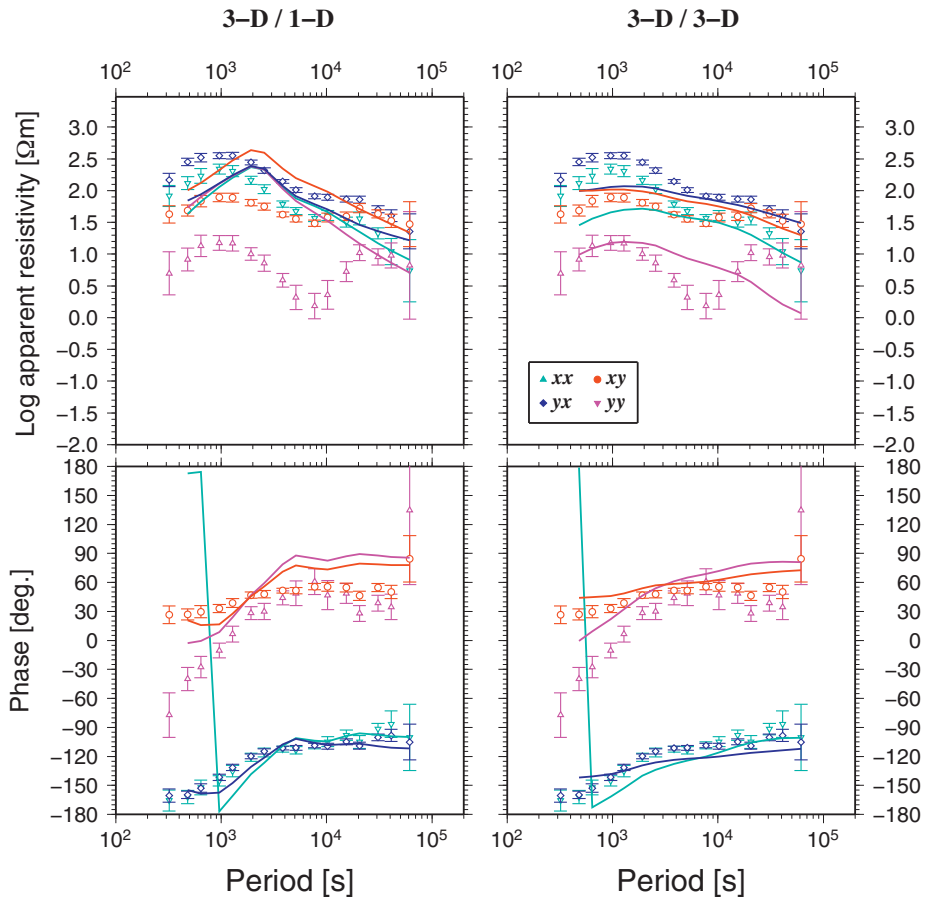
3–D / 1–D

3–D / 3–D

Fig. 11. Forward modeling results for T16. Symbols with error bars are the observed MT responses in both left and right panels. Lines are the responses predicted from 3-D surface heterogeneity over the preferred 1-D model (left) and 3-D heterogeneity over a 3-D mantle in which the two preferred models for the Philippine Sea and Pacific mantles are combined (right).
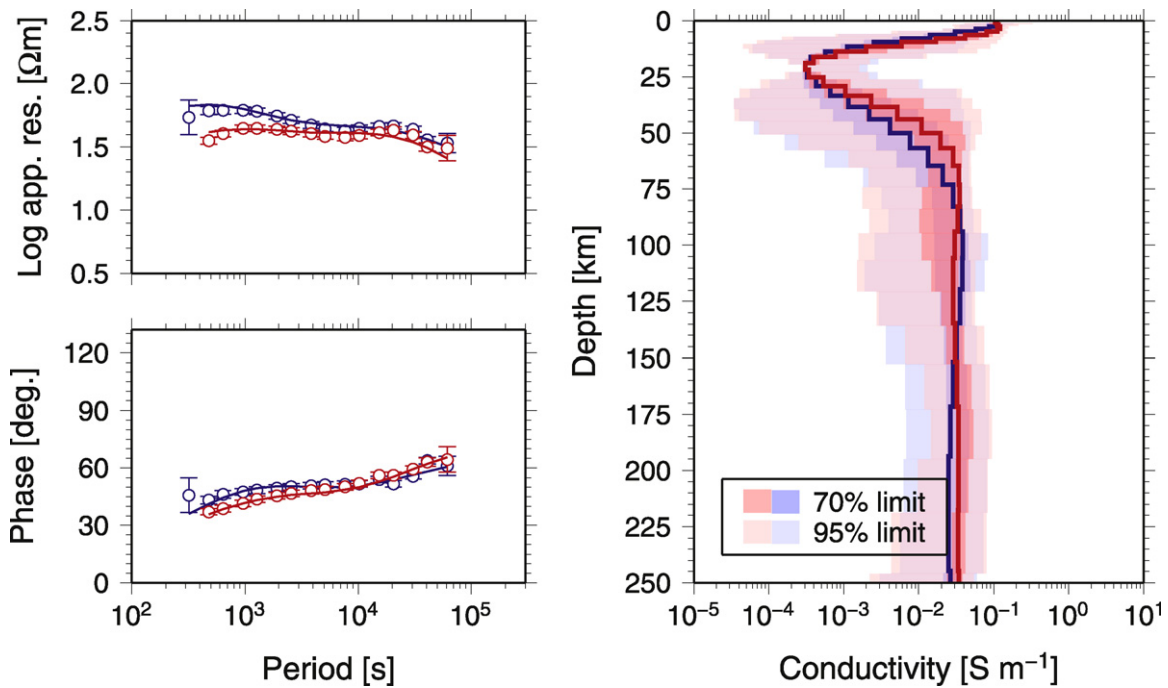

Fig. 12. 1-D inversion results for the averages in the Shikoku–Parece Vela Basin (red) and the West Philippine Basin (blue). Left: Apparent resistivity and phase of $\bar{Z}_{det}$: observed (circles with error bars) and modeled (lines). Right: 1-D conductivity models with uncertainties obtained by the inversions.

north Pacific reference models [the two- and three-jump models of Shimizu et al. (2010a)]. The obtained models for the Philippine Sea and Pacific regions (models D2$_{PHS}$ and D2$_{PAC}$) are plotted in Fig. 10c. Again, the calculated responses to models D2$_{PHS}$ and D2$_{PAC}$ fit the data as well as the responses to the preferred models D0$_{PHS}$ and D0$_{PAC}$ with the RMS misfits of unity. This suggests that the data permit a conductivity as resistive as the north Pacific reference just above the 400 km discontinuity and positive jump in conductivity. The difference in conductivity at 400–550 km between models D2$_{PHS}$ and D2$_{PAC}$ can be distinguished similar to models D1$_{PHS}$ and D1$_{PAC}$, if we see the 70% distribution limits.

The MT data alone cannot constrain the conductivity at around 400 km as shown by the result that the models D0, D1, and D2 depict different conductivity at the depth for different constraints but all models explain the data with the RMS misfit of unity for both the Philippine Sea mantle and the Pacific mantle. However, we are discussing how the data constrain the structure together with the independent information given in each inversion. The robust features observed from a comparison of the models shown in Fig. 10 are the following. The conductivity of the upper half of the MTZ beneath the Philippine Sea region is clearly more conductive than that beneath the Pacific region. The conductivity of the north Pacific reference models tends to fall between the conductivity beneath the two regions. Note that the conductivity at 200–300 km depth looks significantly higher than the north Pacific reference model for both the Philippine Sea and Pacific regions, but they should not be compared. The north Pacific reference models at this depth range are not well constrained by the data because the period range inverted is much longer than that of this study; hence, the top 100 km is *a priori* constrained to be close to 5×10^{-4} S m^{-1} in their inversion analysis (Shimizu et al., 2010a).

The trend of the difference in the conductivity of the upper part of the MTZ between the two regions is possibly consistent with the 3-D inversion of the semi-global longer-period data set of Shimizu et al. (2010b). The conductivity just below 400 km discontinuity is about 0.3 log unit higher for model D2$_{PHS}$ and about 0.7 log unit lower for model D2$_{PAC}$ compared with the reference two-jump model by Shimizu et al. (2010a) (Fig. 10c). The 3-D conductivity anomaly of the uppermost MTZ to the reference two-jump model varies between +0.1 and +0.4 log unit beneath the Philippine Sea and between −0.1 and +0.1 log unit beneath the western edge of the Pacific, respectively (Fig. 10 of Shimizu et al., 2010b). In particular, the high-conductivity anomaly beneath the Philippine Sea is the most robust feature, although the resolution of the mantle below the Pacific is marginal (Shimizu et al., 2010b).

5.4. Quantitative interpretation of the conductivity

The electrical conductivity of mantle-constituting minerals is basically controlled by thermodynamic processes and is expressed as the sum of an Arrhenian-type equation for independent conduction mechanisms,

$$\sigma = \sum_i \sigma_{0i} \exp\left(-\frac{\Delta H_i}{kT}\right), \tag{11}$$

where σ is the electrical conductivity of mineral or melt, $\sigma_{0,i}$ and ΔH_i are the preexponential factor and activation energy for the ith conduction mechanism, respectively, k is the Boltzmann constant, and T is the absolute temperature. Laboratory experiments determine $\sigma_{0,i}$ and ΔH_i from conductivity measurements at various temperatures. For proton conduction (the effect of hydrogen dissolved in mineral), these parameters may be obtained by a water content function (e.g., Wang et al., 2006; Yoshino et al., 2008). Once these parameters are obtained for a mineral, the electrical conductivity can be calculated for a given temperature, and inversely,

temperature can be calculated for a given conductivity, using (11). For hydrated minerals, the water content can be calculated given the conductivity and temperature.

The electrical conductivity model obtained in this study may be transformed into thermal structure, water content in olivine, or fraction of partial melt under some assumptions, using the results of experimental studies. Here, we assume that the conductivity of the upper mantle is represented by the conductivity of olivine, which is the most abundant mineral. We first transform the conductivity into temperature under dry conditions. Second, we transform the conductivity into water content in olivine assuming the thermal structure. Finally, we discuss the condition of partial melting and the melt fraction assuming peridotitic composition.

5.4.1. Thermal structure

Thermal structure models for the Philippine Sea and Pacific mantles were obtained from the preferred conductivity models D0$_{PHS}$ and D0$_{PAC}$ (Fig. 10a) using an experimental model for dry olivine conductivity obtained by Constable (2006) (Figs. 13 and 14, respectively). The resultant thermal models can be regarded as an upper limit of the estimation because any additional effects of the assumed conditions will increase the conductivity and therefore decrease the temperature estimate. The thermal structures predicted from a cooling model are also plotted in Figs. 13 and 14. The predicted models for 20 and 145 Ma oceanic upper mantle, which represent the two observation areas, were calculated based on half-space cooling with a potential temperature of 1350 °C superimposed on a 0.3 °C km^{-1} adiabatic thermal gradient. For both regions, the thermal structures converted from the conductivity are higher than the predictions. However, their depth dependence is similar to the predicted thermal structures.

Some studies have noted that the half-space cooling model does not fit the bathymetric subsidence, heat flow, and geoid height for oceanic lithosphere older than approximately 80 Ma; instead, cooling of a plate with finite thickness and constant temperature at the bottom was introduced to explain these observations (e.g., Parsons and Sclater, 1977; Stein and Stein, 1992). However, the thermal structure obtained from the conductivity for the Pacific mantle is rather cooler than these proposed plate cooling models at a depth of 100–170 km. It is barely valid even for the 95% upper limit of the temperature estimation at 130–170 km depth (Fig. 14). This result indicates that the electrical conductivity may be explained more accurately by the half-space cooling geothermal model with other factors enhancing the conductivity, as discussed in the following sections.

5.4.2. Mantle hydration

The fact that the estimated temperature is higher than the half-space cooling model should be explained by the effect of other parameters enhancing the conductivity, although an actual temperature anomaly should not be ruled out. Hydrogen dissolved in mantle minerals is considered to be one of the most promising candidates for the high-conductivity asthenosphere because Karato (1990) predicted its effect. Some water is actually observed in mid-ocean ridge basalts, indicating that the source mantle reserves some amount of water (e.g., Michael, 1988). Recently, Wang et al. (2006) and Yoshino et al. (2006) measured the conductivity of hydrous olivine; thus, we can estimate the water content in olivine from conductivity observations using their experimental results. However, the two groups reported significantly different impacts of hydration on conductivity.

The water content in olivine is calculated from the conductivity assuming the geothermal structure predicted from the half-space cooling model. We applied the cooling models for 20 and 145 Ma shown for the Philippine Sea mantle and the Pacific mantle, respectively (Figs. 13 and 14). Water content is obtained based on Wang
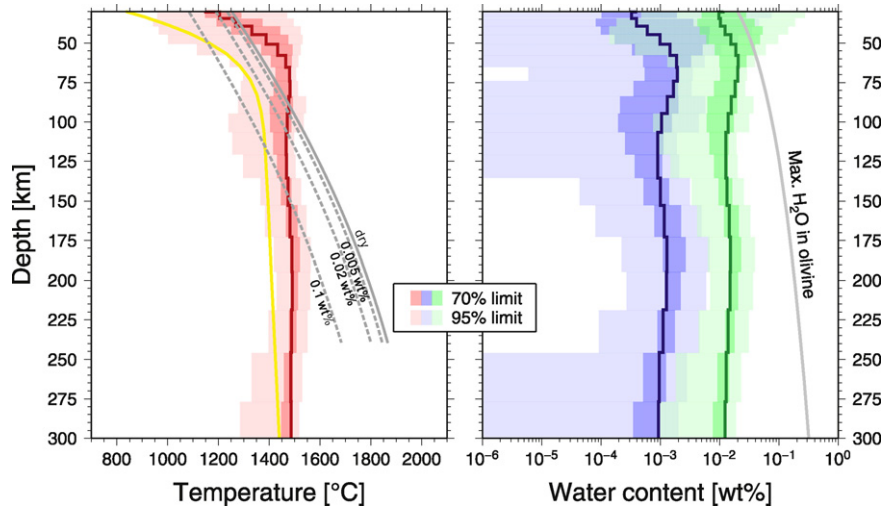
Fig. 13. Temperature and water content estimated from the 1-D conductivity structure for the Philippine Sea mantle. Left: thermal structures converted from the preferred conductivity model $D0_{PHS}$ with uncertainty (red line and shading) and predicted from the half-space cooling model for 20 Ma oceanic lithosphere (yellow line). Solidi of mantle peridotite with various water contents (Aubaud et al., 2004) are also shown (black solid and dashed lines). Right: water content in olivine calculated from $D0_{PHS}$. The half-space cooling model plotted on the left is assumed as the thermal structure for the calculation. Two competing experimental conductivity models for hydrous olivine (Wang et al., 2006; Yoshino et al., 2006) are used (blue and green lines and shading, respectively). Gray line indicates the maximum water content in olivine given by Hirschmann et al. (2005).

et al. (2006) and Yoshino et al. (2006). The obtained water contents differ significantly depending on the experimental result used. For the Philippine Sea mantle, the water content within the 70% limit is estimated to be 0.00014–0.0027 and 0.0059–0.023 wt% at 100–300 km depth for the respective cases. The water content for the Pacific mantle is similar to that for the Philippine Sea mantle at 230–300 km depth because the conductivities are similar. At a depth of 130–230 km, the estimated water content increases with depth. Note that the estimated water content limits exceed the maximum solubility of water in olivine given by Hirschmann et al. (2005) at shallower depth; thus, the values are not applicable.

5.4.3. Partial melting

The condition of partial melting at the expected asthenospheric depth can be examined by comparing the thermal structure with the phase diagram for the upper mantle material. Kawakatsu et al. (2009) found seismic evidence for a sharp lithosphere–asthenosphere boundary beneath the Philippine Sea and northwestern Pacific and interpreted the data in terms of partial melting. Constraining the physical conditions of the asthenosphere is a long-standing problem, and discussing it in terms of electrical conductivity is definitely important.

The thermal structure converted from the conductivity model $D0_{PHS}$ under dry conditions is higher than the dry solidus of mantle peridotite given by Aubaud et al. (2004), as shown in Fig. 13. This means that the mantle can be partially molten at depths 40–80 km beneath the Philippine Sea if it is dry. The dry solidus is 1400 °C at approximately 65 km depth. Using this temperature, an experimental conductivity model for basaltic melt obtained by Tyburczy and Waff (1983), and a mixing law of the conductivity for the two phases
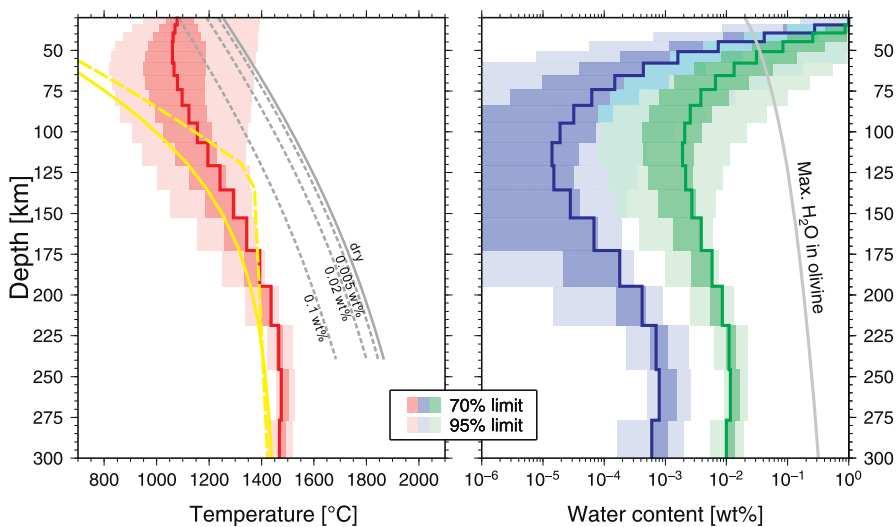

Fig. 14. Temperature and water content estimated from the 1-D conductivity structure for the Pacific mantle. Left: thermal structures converted from the preferred conductivity model $D0_{PAC}$ with uncertainty (red line and shading) and predicted from the half-space cooling model (yellow solid line) and from the plate cooling model based on Parsons and Sclater (1977) (yellow dashed line) for 145 Ma oceanic lithosphere. Solidi of mantle peridotite with various water contents (Aubaud et al., 2004) are also shown (black solid and dashed lines). Right: water content in olivine calculated from $D0_{PAC}$. The half-space cooling model plotted on the left is assumed as the thermal structure for the calculation. Two competing experimental conductivity models for hydrous olivine (Wang et al., 2006; Yoshino et al., 2006) are used (blue and green lines and shading, respectively). Gray line indicates the maximum water content in olivine given by Hirschmann et al. (2005).

(dry olivine and basaltic melt) by Hashin and Shtrikman (1962), the melt fraction can be estimated from the conductivity. The obtained melt fraction is 0.5%, which falls in the range estimated from seismic data (Kawakatsu et al., 2009). Even if the mantle is hydrated, partial melt may occur at around 75 km depth if we adopt the experimental result of Yoshino et al. (2006). Around that depth, the estimated water content is 0.020 wt% (95% upper limit is 0.028 wt%) (Fig. 13, right), and the solidus of peridotite for a water content of 0.02 wt% (Aubaud et al., 2004) is very close to the half-space cooling model assumed for the water content calculation (Fig. 13, left). However, partial melting will not occur if the effect of hydrogen on the conductivity is as low as Wang et al. (2006) reported, because even the upper 95% limit of the estimated water content is as small as 0.0034 wt%, and thus the corresponding solidus is approximately 80 °C higher than the assumed thermal structure model.

For the Pacific mantle, on the other hand, the present model study suggests that the data do not require the presence of partial melting at asthenospheric depth assuming peridotitic composition. Even the higher estimate of the water content is <0.022 wt% at 100–300 km depth. This amount of water cannot reduce the solidus temperature to the assumed range (Fig. 14). The 1-D conductivity model indicates the mean structure beneath the observation area, and lateral variations should exist. However, such heterogeneity is probably too small to introduce partial melting locally, as indicated by the relative uniformity of the observed MT responses. The inversion with a smoothness constraint searches a limited space of possible conductivity models, so acceptable models may exist, which include a thin conductive layer that allows partial melting with the existence of some water. Although we may be unable to discuss the Pacific mantle any further because of the still-limited number of observation sites, the present result suggests that the conditions for partial melting are rather restricted compared with the Philippine Sea mantle.

6. Conclusions

We conducted iterative observations using OBEMs in 2005–2008 as a part of the SSP to attempt to image the electrical conductivity structure of a stagnant slab and the surrounding mantle. Data were successfully collected from a total of 37 instruments deployed at 18 sites.

Reference 1-D models for the electrical conductivity of the upper mantle beneath the Philippine Sea and the westernmost Pacific were created by analyzing the SSP data and eight data sets collected by past experiments. The effect of the surface heterogeneity structure on the data was carefully corrected, and the corrected data were inverted. This procedure was iterated three times to examine the coupling effect with the mantle conductivity structure. During this analysis, the conductivity for the lithospheric mantle was constrained to $3.2 \times 10^{-4}\,\mathrm{S\,m^{-1}}$.

The obtained 1-D models indicate that (1) the resistive layer beneath the Philippine Sea is much thinner than that for the Pacific mantle, supporting the large difference in representative lithospheric age of each area, (2) mantle conductivity at depths of 200–300 km is relatively more uniform at approximately 0.3 S m^{-1} for both regions, and (3) the conductivity just below 400 km depth is higher for the Philippine Sea mantle than for the Pacific mantle, which is consistent with the semi-global analysis of Shimizu et al. (2010b).

The 1-D conductivity models are interpreted on the basis of experimental results for the conductivity of olivine with some assumptions. The thermal structure reproduced from the conductivity under dry conditions is higher than the half-space cooling model. The water content differs considerably between cases adopting the experimental results of Wang et al. (2006) and those of

Yoshino et al. (2006). Partial melting of 0.5% can exist at 40–80 km depth beneath the Philippine Sea because the estimated temperature is higher than the dry solidus of mantle peridotite. If the higher estimate of the water content based on Yoshino et al. (2006) is applied, the solidus may be lower than the temperature predicted for the half-space cooling model at a depth around 75 km. In conclusion, the present analysis suggests that partial melting is possible beneath the Philippine Sea but is not required beneath the western Pacific region even if we consider the hydration of the mantle.

Appendix A. 3-D surface heterogeneity modeling

A.1. Combination of local and regional topographic effects

The survey area is larger than the scale of local topography, which affects the observed EM fields, and modeling such small and large structures simultaneously requires a huge number of grid cells, and thus extreme computation performance. Baba and Seama (2002) developed a new technique to express topographic change; it does not express the topographic relief with a number of fine grid cells but transforms the topographic relief into a change in electrical conductivity and magnetic permeability within a locally flat seafloor with a moderate number of grid cells. We used their method to simulate the MT responses to save computer resources and computing time. Nonetheless, modeling the entire observation area at once is very resource intensive. Therefore, it is realistic to approximate the total fields by combining the fields calculated for two different scale models in which a large (small) area is discretized by a larger (smaller) mesh.

In this study, following Yoneda (2008), we calculate the EM fields for a regional large-scale topography including an ocean-land distribution ($\mathbf{E}_{regional}$ and $\mathbf{H}_{regional}$) and those for local small-scale topography at each site ($\mathbf{E}_{local}$ and $\mathbf{H}_{local}$) by 3-D forward modeling. The total fields ($\mathbf{E}_{total}$ and $\mathbf{F}_{total}$) are approximated by a linear combination of the fields for regional and local topography together with the normal field ($\mathbf{E}_{normal}$ and $\mathbf{H}_{normal}$), which is the field for only the 1-D mantle structure,

$$\mathbf{E}_{total} \approx \mathbf{E}_{apparent} = \mathbf{E}_{regional} + \mathbf{E}_{local} - \mathbf{E}_{normal}, \tag{A.1}$$

$$\mathbf{H}_{total} \approx \mathbf{H}_{apparent} = \mathbf{H}_{regional} + \mathbf{H}_{local} - \mathbf{H}_{normal}. \tag{A.2}$$

The MT impedance at a site is calculated from $\mathbf{E}_{apparent}$ and $\mathbf{H}_{apparent}$.

The regional fields are modeled for a 3-D model consisting of the surface heterogeneity discretized as shown in Fig. 4 and a 1-D mantle structure. The mesh size is 30 km × 30 km in the central area. The topography in the 150 km × 150 km area centered on each site is flattened by the average of the area. Regional fields for all sites are calculated by one-forward modeling. For the local topography, data based on multi-narrow-beam sounding are modeled in a 150 km × 150 km area around sites by a finer mesh (1 km × 1 km
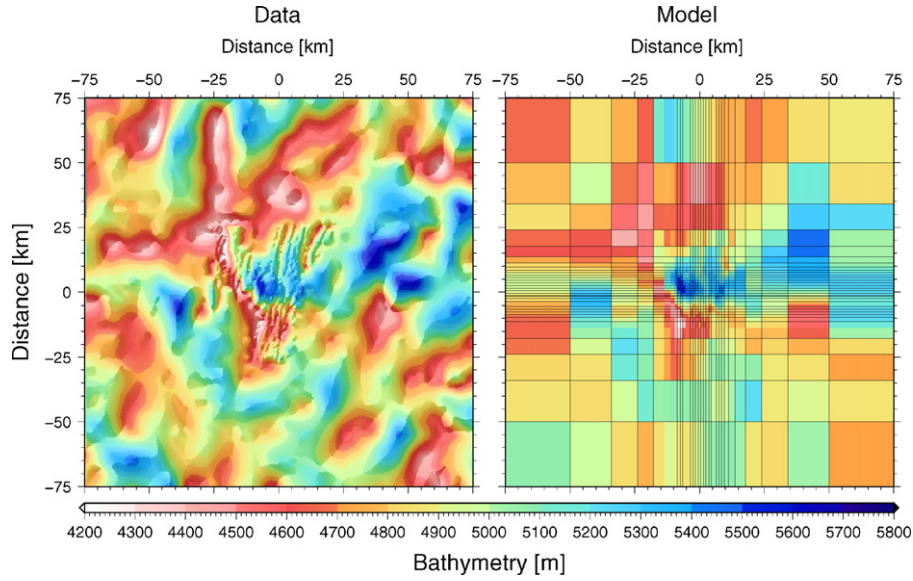
Fig. 15. Local small-scale topography data (left) and model (right) for T10. Data are created by combining the ETOPO2 and multi-narrow-beam sounding data.

in the vicinity of the site). The area without the multi-narrow-beam sounding data is filled by ETOPO2 data. Fig. 15 shows an example of the local topography model for T10. The local fields are simulated for a 3-D model consisting of the local topography and 1-D mantle structure. This modeling is conducted for each site.

Fig. 16 shows the MT responses at T10 calculated from the EM field simulated for the regional and local 3-D models and normal (1-D) model ($\mathbf{Z}_{regional}$, $\mathbf{Z}_{local}$, $\mathbf{Z}_{normal}$). Because of the local topography, the yx response deviates more from the 1-D responses with decreasing period. The diagonal apparent resistivities monotonically decrease with increasing period. The off-diagonal apparent resistivities of the regional response are smaller than those of the 1-D response, but the diagonal apparent resistivities are larger in longer periods.

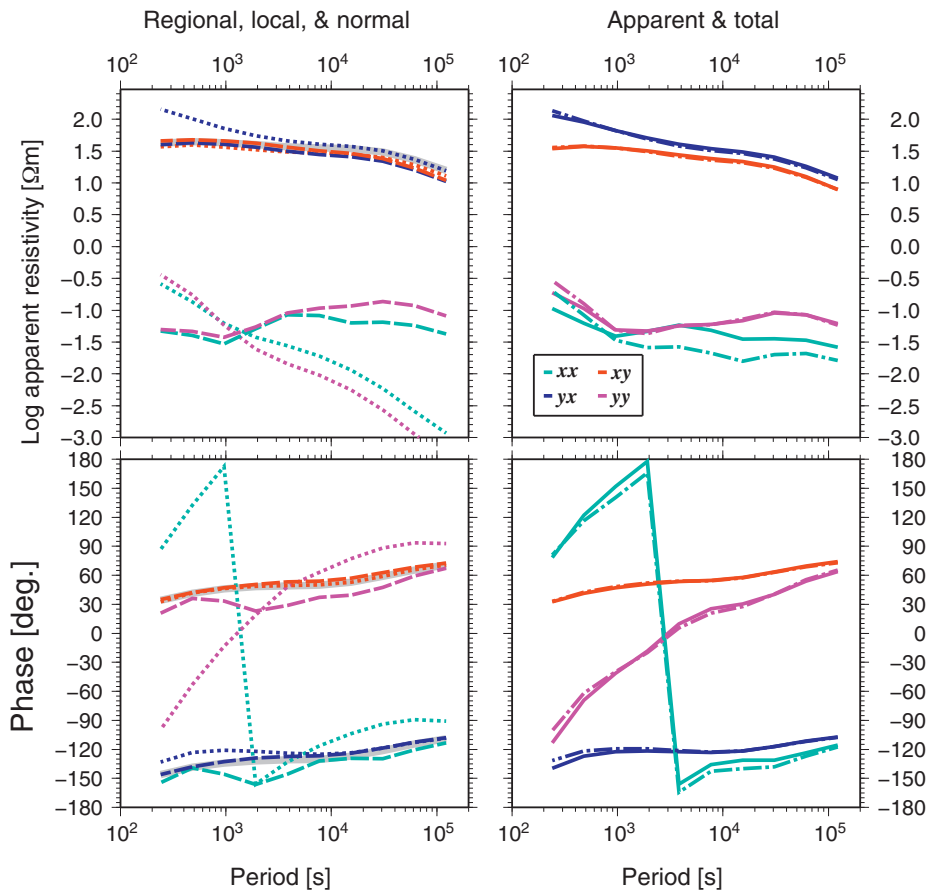**Fig. 16.** Comparison of the apparent resistivity and phase at T10. The left panel gives four elements of the responses for $\mathbf{Z}_{regional}$ (colored dashed lines), $\mathbf{Z}_{local}$ (colored dotted lines), and $\mathbf{Z}_{normal}$ (gray solid lines), and the right panel gives those for $\mathbf{Z}_{apparent}$ (colored solid lines) and $\mathbf{Z}_{total}$ (colored dot-dashed lines).

The MT response $\mathbf{Z}_{apparent}$ was calculated from the combined EM fields ($\mathbf{E}_{apparent}$ and $\mathbf{H}_{apparent}$) and compared with the response $\mathbf{Z}_{total}$ calculated by brute force forward modeling of a large area with a smaller mesh in the central area to demonstrate the validity of the combination method (Fig. 16, right). The apparent resistivity and phase for $\mathbf{Z}_{apparent}$ and $\mathbf{Z}_{total}$ are very similar. Small differences appear, but they are almost within the observation errors. Consequently, we can conclude that $\mathbf{Z}_{total}$ can be approximated by $\mathbf{Z}_{apparent}$.

A.2. Horizontal dimension of the 3-D model

We performed forward modeling to check whether the horizontal dimension is large enough to avoid boundary effects in simulating the surface heterogeneity effect on the MT responses in the survey area. The topography in the smaller 6080 km × 6080 km area shown by a red box in Fig. 4 was incorporated into the surface model and combined with the same 1-D model as model L3. The MT responses of the sites on the Philippine Sea plate and the RMS misfit to the observed responses were calculated. The resultant misfit is 14.4, which is the same as the misfit for model L3 (Table 2). This indicates that the 10,000 km × 10,000 km area is large enough to accurately simulate the regional topographic effect.

A.3. Conductivity of land crust

The conductivity of the land crust is assumed to be 0.01 S m^{-1} in the forward modeling, and the surface heterogeneity effect on the seafloor MT responses depends on its value. To examine its validity, we conducted additional forward modeling for two models in which the conductivity of the land crust is set to 0.1 S m^{-1} (C1) and 0.001 S m^{-1} (C2). The same 1-D mantle structure as model L3 was applied to both. We obtained an RMS misfit of 14.9 for model C1 and 14.3 for model C2. The latter RMS misfit is close to the value for the model with 0.01 S m^{-1} crust, 14.4. The differences in the RMS misfits are smaller than the differences for models with different conductivity for lithospheric mantle demonstrated in Section 3.2, suggesting that the impact of the conductivity of the land crust on the MT responses is secondary. We conclude that the assumed value of 0.01 S m^{-1} is valid for modeling the surface heterogeneity effect in this study.

References

Aubaud, C., Hauri, E.H., Hirschmann, M.M., 2004. Hydrogen partition coefficients between nominally anhydrous minerals and basaltic melts. Geophys. Res. Lett. 31, L20611, doi:10.1029/2004GL021341.

Baba, K., Chave, A.D., 2005. Correction of seafloor magnetotelluric data for topographic effects during inversion. J. Geophys. Res. 110, B12105, doi:10.1029/2004JB003463.

Baba, K., Seama, N., 2002. A new technique for the incorporation of seafloor topography in electromagnetic modelling. Geophys. J. Int. 150, 392–402.

Baba, K., Seama, N., Goto, T., Ichiki, M., Schwalenberg, K., Utada, H., Suyehiro, K., 2005. Electrical structure of the upper mantle in the Mariana subduction system, IFREE report 2003–2004. Frontier Research on Earth Evolution, 2.

Caldwell, T.G., Bibby, H.M., Brown, C., 2004. The magnetotelluric phase tensor. Geophys. J. Int. 158, 457–469, doi:10.1111/j.1365-246X.2004.02281.x.

Chave, A.D., Smith, J.T., 1994. On electric and magnetic galvanic distortion tensor decompositions. J. Geophys. Res. 99 (B3), 4669–4682.

Chave, A.D., Thomson, D.J., 2004. Bounded influence magnetotelluric response function estimation. Geophys. J. Int. 157, 988–1006, doi:10.1111/j.1365-246X.2004.02203.x.

Constable, S., 2006. SEO3: a new model of olivine electrical conductivity. Geophys. J. Int. 166, 435–437, doi:10.1111/j.1365-246X.2006.03041.x.

Constable, S., Cox, C.S., 1996. Marine controlled-source electromagnetic sounding. 2. The PEGASUS experiment. J. Geophys. Res. 101 (B3), 5519–5530.

Constable, S.C., Parker, R.L., Constable, C.G., 1987. Occam's inversion: a practical algorithm for generating smooth models from electromagnetic sounding data. Geophysics 52 (3), 289–300.

Cox, C.S., Constable, S.C., Chave, A.D., Webb, S.C., 1986. Controlled-source electromagnetic sounding of the oceanic lithosphere. Nature 320, 52–54.

Fukao, Y., Widiyantoro, S., Obayashi, M., 2001. Stagnant slabs in the upper and lower mantle transition region. Rev. Geophys. 39, 291–323.

Fukao, Y., Koyama, T., Obayashi, M., Utada, H., 2004. Trans-Pacific temperature field in the mantle transition region derived from seismic and electromagnetic tomography. Earth Planet. Sci. Lett. 217, 425–434.

Goto, T., Kasaya, T., Mikada, H., Kinoshita, M., Suyehiro, K., Kimura, T., Ashida, Y., Watanabe, T., Yamane, K., 2003. Electromagnetic survey of fluid distribution and migration—An example at the Nankai seismogenic zone. BUTSURI-TANSA 56 (6), 439–451 (in Japanese).

Hashin, Z., Shtrikman, S., 1962. A Variational approach to the theory of the effective magnetic permeability of multiphase materials. J. Appl. Phys. 33 (10), 3125–3131.

Heinson, G.S., Lilley, F.E.M., 1993. An application of thin-sheet electromagnetic modelling to the Tasman Sea. Phys. Earth Planet. Int. 81, 231–251.

Hirschmann, M.M., Aubaud, C., Withers, A.C., 2005. Storage capacity of H_2O in nominally anhydrous minerals in the upper mantle. Earth Planet. Sci. Lett. 236, 167–181, doi:10.1016/j.epsl.2005.04.022.

International Association of Geomagnetism and Aeronomy (IAGA), Division V, Working Group VMOD: Geomagnetic Field Modeling, 2005. The 10th-generation of international geomagnetic reference field. Geophys. J. Int. 161, 561–565, doi:10.1111/j.1365-246X.2005.02641.x.

Ichiki, M., Baba, K., Obayashi, M., Utada, H., 2006. Water content and geotherm in the upper mantle above the stagnant slab: interpretation of electrical conductivity and seismic P-wave velocity models. Phys. Earth Planet. Int. 155, 1–15, doi:10.1016/j.pepi.2005.09.010.

Karato, S., 1990. The role of hydrogen in the electrical conductivity of the upper mantle. Nature 347, 272–273.

Kasaya, T., Goto, T., Mikada, H., Baba, K., Suyehiro, K., Utada, H., 2005. Resistivity image of the Philippine Sea Plate around the 1944 Tonankai earthquake zone deduced by Marine and Land MT surveys. Earth Planets Space 57, 209–213.

Kasaya, T., Goto, T., Baba, K., Utada, H., Toh, H., Seama, N., Nogi, Y., Ichiki, M., Ichikita, T., Ohnishi, N., in preparation, Development of a long-term Ocean bottom electro-magnetometer and evaluation using the three years data.

Kawakatsu, H., Kumar, P., Takei, Y., Shinohara, M., Kanazawa, T., Araki, E., Suyehiro, K., 2009. Seismic evidence for sharp lithosphere-asthenosphere boundaries of oceanic plates. Science 324, 499–502, doi:10.1126/science.1169499.

Lizarralde, D., Chave, A., Hirth, G., Schultz, A., 1995. Northeastern Pacific mantle conductivity profile from long-period magnetotelluric sounding using Hawaii-to-California submarine cable data. J. Geophys. Res. 100 (B9), 17837–17854.

Matsuno, T., Seama, N., Evans, R.L., Chave, A.D., Baba, K., White, A., Goto, T., Heinson, G., Boren, G., Yoneda, A., Utada, H., 2010. Upper mantle electrical resistivity structure beneath the central Mariana subduction system. Geochem. Geophys. Geosyst. 11 (9), Q09003, doi:10.1029/2010GC003101.

Michael, P.J., 1988. The concentration, behavior and storage of H_2O in the suboceanic upper mantle: implications for mantle metasomatism. Geochem. Cosmochim. Acta 52, 555–566.

Müller, R.D., Sdrolias, M., Gaina, C., Roest, W.R., 2008. Age, spreading rates, and spreading asymmetry of the world's ocean crust. Geochem. Geophys. Geosyst. 9 (4), doi:10.1029/2007GC001743.

National Geophysical Data Center, National Oceanic and Atmospheric Administration, U.S. Dept. of Commerce, ETOPO2v2 Global Gridded 2-minute Database, http://www.ngdc.noaa.gov/mgg/global/etopo2.html.

Nolasco, R., Tarits, P., Filloux, J.H., Chave, A.D., 1998. Magnetotelluric imaging of the Society Islands hotspot. J. Geophys. Res. 103 (B12), 30287–30309.

Obayashi, M., Yoshimitsu, J., Fukao, Y., 2009. Tearing of stagnant slab. Science 324, 1173–1175, doi:10.1126/science.1172496.

Parker, R.L., Booker, J.R., 1996. Optimal one-dimensional inversion and bounding of magnetotelluric apparent resistivity and phase measurements. Phys. Earth Planet. Int. 98, 269–282.

Parsons, B., Sclater, J.G., 1977. An analysis of the variation of ocean floor bathymetry and heat flow with age. J. Geophys. Res. 82 (5), 803–827.

Seama, N., Baba, K., Utada, H., Toh, H., Tada, N., Ichiki, M., Matsuno, T., 2007. 1-D electrical conductivity structure beneath the Philippine Sea: results from an ocean bottom magnetotelluric survey. Phys. Earth Planet. Int. 162, 2–12, doi:10.1016/j.pepi.2007.02.014.

Shimizu, H., Koyama, T., Baba, K., Utada, H., 2010a. Revised 1-D mantle electrical conductivity structure beneath the north Pacific. Geophys. J. Int. 180, 1030–1048, doi:10.1111/j.1365-246X.2009.04466.x.

Shimizu, H., Utada, H., Baba, K., Koyama, T., Obayashi, M., Fukao, Y., 2010b. Three-dimensional imaging of electrical conductivity in the mantle transition zone beneath the North Pacific Ocean by a semi-global induction study. Phys. Earth Planet. Int., doi:10.1016/j.pepi.2010.01.010.

Shiobara, H., Baba, K., Utada, H., Fukao, Y., 2009. Ocean bottom array probes stagnant slab beneath the Philippine Sea. Eos Trans. AGU 90 (9), 70–71.

Stein, C.A., Stein, S., 1992. A model for the global variation in oceanic depth and heat flow with lithospheric age. Nature 359, 123–129.

Swift Jr., C.M., 1967. A magnetotelluric investigation of an electrical conductivity anomaly in the southwestern United States. Ph.D. thesis, Mass. Inst. of Tech.

Toh, H., 1993. Electrical conductivity structure of the Izu-Bonin arc revealed by seafloor electromagnetic observations. Ph.D. thesis, University of Tokyo.

Toh, H., Hamano, Y., Ichiki, M., 2006. Long-term seafloor geomagnetic station in the northwest Pacific: A possible candidate for a seafloor geomagnetic observatory. Earth Planets space 58, 697–705.

Tyburczy, J.A., Waff, H.S., 1983. Electrical conductivity of molten basalt and andesite to 25 kilobars pressure: geophysical significance and implications for charge transport and melt structure. J. Geophys. Res. 88 (B3), 2413–2430.

Utada, H., Hamno, Y., Yukutake, T., 1986. A two-dimensional conductivity model across central Japan. J. Geomag. Geoelectr. 38, 447–473.

Utada, H., Hamano, Y., Segawa, J., 1996. Conductivity anomaly around the Japanese islands. In: Isezaki, N., et, al. (Eds.), Geology and Geophysics of the Japan Sea. Japan-USSR Monogr. Ser. 1, Terra Sci. Publ. Co. Ltd., pp. 103–149.

Utada, H., Hibiya, N., Uyeshima, M., Shimizu, H., Mikada, H., Goto, T., Kawaguchi, K., 2005. An experimental study of the Earth's electric field. Report of grant-in-aid for scientific research, No.14204041 (in Japanese).

Utada, H., Koyama, T., Obayashi, M., Fukao, Y., 2009. A joint interpretation of electromagnetic and seismic tomography models suggests the mantle transition zone below Europe is dry. Earth Planet. Sci. Lett. 281, 249–257, doi:10.1016/j.epsl.2009.02.027.

Utada, H., Yoneda, A., Shimizu, H., Baba, K., Palshin, N., 2008. Effect of Sq variations on the electromagnetic response functions in the period range between 3 hours and 1 day. In: Abstract for 19th international workshop on electromagnetic induction in the Earth, Beijing, China.

Wang, D., Mookherjee, M., Xu, Y., Karato, S., 2006. The effect of water on the electrical conductivity of olivine. Nature 443, 977–980, doi:10.1038/nature05256.

Wessel, P., Smith, W.H.F., 1998. New, improved version of the generic mapping tools released. Eos Trans. AGU 79, 579.

Xu, Y., Shankland, T.J., Poe, B.T., 2000. Laboratory-based electrical conductivity in the Earth's mantle. J. Geophys. Res. 105 (B12), 27865–27875.

Yamazaki, T., Seama, N., Okino, K., Kitada, K., Joshima, M., Oda, H., Naka, J., 2003. Spreading process of the northern Mariana Trough: rifting-spreading transition at 22°N. Geochem. Geophys. Geosyst. 4 (9), 1075, doi:10.1029/2002GC000492.

Yoneda, A., 2008. On topographic effect in seafloor elegromagnetic response functions. Ms. thesis, University of Tokyo, in Japanese.

Yoshino, T., Matsuzaki, T., Yamashita, S., Katsura, T., 2006. Hydrous olivine unable to account for conductivity anomaly at the top of the asthenosphere. Nature 443, 973–976, doi:10.1038/nature05223.

Yoshino, T., Manthilake, G., Matsuzaki, T., Katsura, T., 2008. Dry mantle transition zone inferred from the conductivity of wadsleyite and ringwoodite. Nature 451, 326–329, doi:10.1038/nature06427.